

NASA TECHNICAL NOTE



NASA TN D-6584

2.1

NASA TN D-6584

LOAN COPY: RE  
AFWL (DO  
KIRTLAND AF



# DEVELOPMENT OF SKYLAB EXPERIMENT T-013 CREW/VEHICLE DISTURBANCES

*by Bruce A. Conway  
Langley Research Center  
Hampton, Va. 23365*





0133149

1. Report No. NASA TN D-6584		2. Government Accession No.		3. Recipient's Catalog No.	
4. Title and Subtitle DEVELOPMENT OF SKYLAB EXPERIMENT T-013 CREW/VEHICLE DISTURBANCES				5. Report Date January 1972	
				6. Performing Organization Code	
7. Author(s) Bruce A. Conway				8. Performing Organization Report No. L-7985	
9. Performing Organization Name and Address NASA Langley Research Center Hampton, Va. 23365				10. Work Unit No. 948-70-70-13	
				11. Contract or Grant No.	
12. Sponsoring Agency Name and Address National Aeronautics and Space Administration Washington, D.C. 20546				13. Title	
15. Supplementary Notes With appendix A by Charles T. Woolley and appendix B by Peter R. Kurzhals and Robert B. Reynolds.					
16. Abstract <p>A Skylab experiment to determine the characteristics and effects of crew-motion disturbances has been developed. The experiment, designated T-013, will correlate data from histories of specified astronaut body motions, the disturbance forces and torques produced by these motions, and the resultant spacecraft control-system response to the disturbances. Primary application of crew-motion-disturbance data will be to the sizing and design of future manned spacecraft control and stabilization systems. This report presents the development of the crew/vehicle disturbances experiment. Appendixes derive a mathematical model of human body motion which may be used for analysis of a variety of man-motion activities.</p>					
17. Key Words (Suggested by Author(s)) Crew-motion disturbance Attitude control Skylab Analytical model of man			18. Distribution Statement Unclassified - Unlimited		
19. Security Classif. (of this report) Unclassified		20. Security Classif. (of this page) Unclassified		21. No. of Pages 67	22. Price* \$3.00

DEVELOPMENT OF SKYLAB EXPERIMENT T-013  
CREW/VEHICLE DISTURBANCES

By Bruce A. Conway  
Langley Research Center

SUMMARY

A Skylab experiment to determine the characteristics and effects of crew-motion disturbances has been developed. The experiment, designated T-013, will correlate data from histories of specified astronaut body motions, the disturbance forces and torques produced by these motions, and the resultant spacecraft control-system response to the disturbances. Primary application of crew-motion-disturbance data will be to the sizing and design of future manned spacecraft control and stabilization systems. This report presents the development of the crew/vehicle disturbances experiment. Appendixes derive a mathematical model of human body motion which may be used for analysis of a variety of man-motion activities.

INTRODUCTION

Motions of astronaut crew members while in contact with a spacecraft can produce disturbances on the spacecraft which would affect pointing accuracy, or otherwise impose demands on the stabilization and control system. The resultant attitude errors (ref. 1) can be cumulative if the crew-motion path results in a net rotation of crew mass relative to the spacecraft center of mass. In addition, any transient rate and attitude errors are generally sufficiently large to require active control. Sizing of such a control system is dependent on the crew-motion disturbance characteristics. Since crew motions generally represent the largest disturbance torques and forces for manned spacecraft, and the frequencies contained in these torque histories are several orders of magnitude higher than those associated with external disturbances (such as gravity-gradient and aerodynamic moments), the torque level and bandwidth of the control system must be sufficiently large to allow compensation for the crew disturbances. Flexibility modes of the spacecraft and any attached experiment packages may also be excited by crew motions, necessitating definition of frequency content of the disturbances. Simple extrapolation of the sizing requirements of the control system for one-, two-, or three-man crews to account for six-, 12-, or even 50-man crews might result in unnecessarily large, overdesigned systems. Detailed characteristics of crew-motion disturbances including

both discrete and stochastic models of crew-motion forces and torques must thus be developed to permit effective design of future spacecraft and experiment control systems. Accurate knowledge of these characteristics will result in realistic control-system sizing requirements.

Initial studies of crew-motion disturbances considered crew members as point masses, and investigated the effects on a spacecraft of translating one or more of these masses from one point to another within the spacecraft. The studies included digital computer simulations of spacecraft dynamics, along with spin tests using dynamically scaled models of various spacecraft inertia configurations. Following these earlier simulations, consideration of man, himself, as a dynamic system was begun. Development of an anthropometric model of the human body was carried out, using earlier U.S. Air Force anthropometric studies (refs. 2 to 6). This anthropometric model was extended to include the dynamics of body-segment motions. The resultant analytical model may be used to compute crew-disturbance forces and torques in a spacecraft and the spacecraft response, for specified astronaut motions. Efforts carried out by Hendricks, Johnson, and Kirch (ref. 7) have developed stochastic representations of crew-motions-disturbance forces and moments for selected crew activities, with applications to control-system frequency-response investigations.

Use of both discrete and stochastic techniques developed to describe crew-motion disturbances requires verification of these techniques by experimentation. Several techniques of simulating the zero-gravity environment of a manned spacecraft and their primary advantages with respect to a crew-motion experiment are listed in table I. Because of the limitations of ground-based simulations and, consequently, the questionable applicability of resultant data, a manned space flight experiment was proposed to be flown aboard the Skylab spacecraft. The Skylab orbital workshop (see fig. 1) provides an excellent laboratory for crew disturbance research, since it is primarily an experiment carrier, and hence has facilities to provide maximum experiment support.

This report will discuss the development of a manned spaceflight experiment whose objectives are (1) to determine the characteristics of typical crew-motion disturbances and (2) to assess the response of a representative manned spacecraft control system to some of these disturbances. The resultant experiment, designated Skylab experiment T-013, will be described with respect to its implementation hardware and protocol. Included in the report as pertinent to the development of experiment T-013 are two appendixes: Appendix A, by Charles T. Woolley, presents the derivation of the physical properties for the anthropometric model of man; appendix B, by Peter R. Kurzhals and Robert B. Reynolds, derives the dynamic equations associated with motions of the anthropometric model.

TABLE I.- SEVERAL ZERO-GRAVITY SIMULATION TECHNIQUES

Simulation approach	Advantages	Disadvantages
Underwater neutral buoyancy	Approximates actual zero-g for unsuited subject	Drag excessive for all but slowest motions Breathing equipment restrictive
Air bearing simulation	Provides good low- or zero-g effect in two dimensions	Implementation of force measuring techniques difficult Requires extremely fine balance and c.g. shift compensation Must counteract gravity in many motions Mounting harnesses, etc., too restrictive Susceptible to ambient air movement
Servo-drive simulation (ref. 8)	Can be tied together directly with computer simulation of spacecraft dynamics	Must counteract gravity in many motions Mounting harnesses too restrictive
Cable suspension	Relatively low cost	Degrees of freedom limited Pendulum effects present Support apparatus restrictive
Zero-g aircraft	Actual zero-g environment	Short run times Unnatural positive-g forces interspersed between zero-g runs

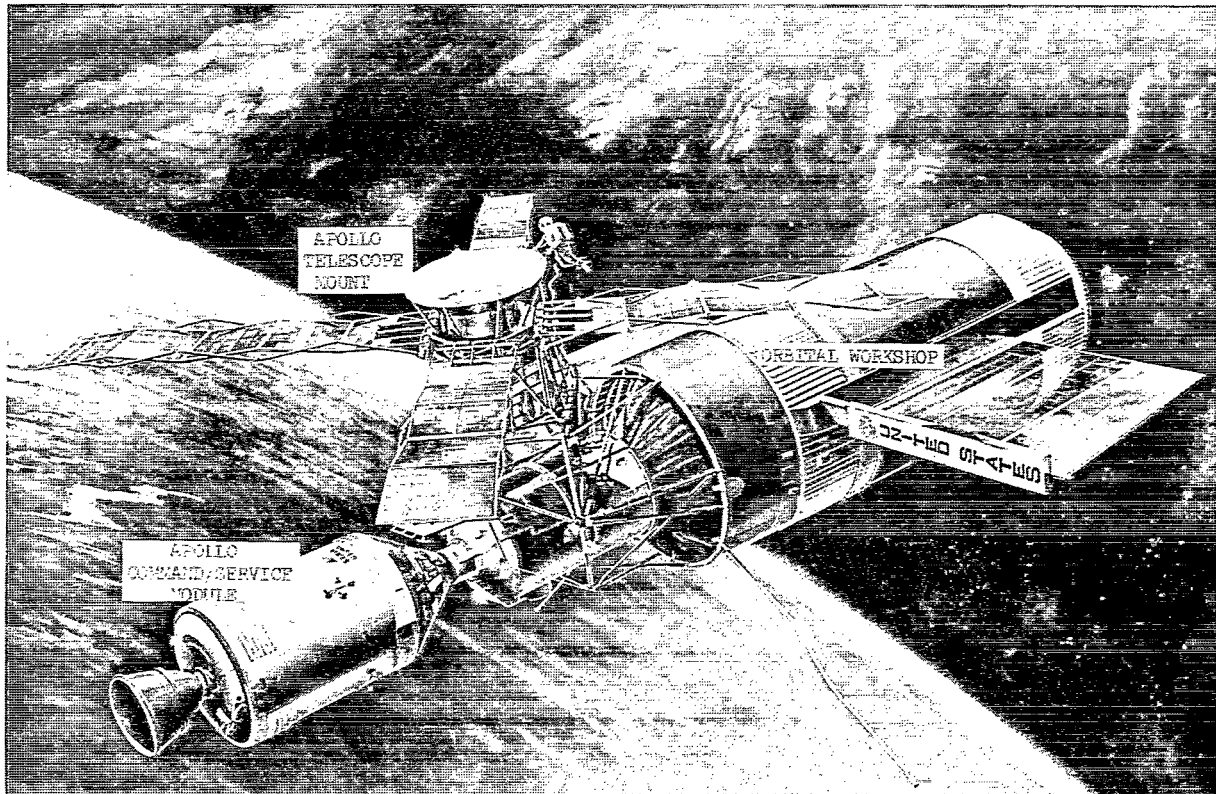


Figure 1.- Skylab orbital assembly.

### SYMBOLS

AA, BB	functions of conical frustum dimensions, used in moment-of-inertia computations
BF	total mass of both feet of model man
BFO	total mass of both forearms of model man
BH	total mass of both hands of model man
BLL	total mass of both lower legs of model man
BUA	total mass of both upper arms of model man
BUL	total mass of both upper legs of model man
HNT	total mass of head, neck, and trunk of model man

$[D]$	Euler angle transformation matrix
d	element of $[D]$
DELSH	lower torso hinge point location with respect to bottom of torso of model man
F	force
$F_1, F_2, \dots, F_6$	force in load cell 1, 2, . . . , 6
H	angular momentum
I	moment of inertia
k	location of load-cell-array centroid
M	moment
m	mass
$m_T'$	corrected total mass of model man
Q	mass factor (see eq. (B11))
$\{R\}, \{r\}$	position radius vectors (see fig. 36)
$\left. \begin{array}{l} R \\ RR \\ SL \\ SR \\ SML \\ SMR \end{array} \right\}$	model-man segment dimensions defined in appendix A (see figs. 18 to 30)
$SI_{XX}, SI_{YY}, SI_{ZZ}$	model-man segment moments of inertia
S.D.	standard deviation
T	torque

t	time
V	volume
X,Y,Z	coordinate axes of spacecraft body
X <sub>F</sub> ,Y <sub>F</sub> ,Z <sub>F</sub>	inertially fixed axes
X <sub>I</sub> ,Y <sub>I</sub> ,Z <sub>I</sub>	intermediate spacecraft axes (see fig. 36)
X <sub>M</sub> ,Y <sub>M</sub> ,Z <sub>M</sub>	model-man center-of-mass body axes
X <sub>MI</sub> ,Y <sub>MI</sub> ,Z <sub>MI</sub>	model-man reference axes
X <sub>MS</sub> ,Y <sub>MS</sub> ,Z <sub>MS</sub>	model-man center-of-mass axes parallel to spacecraft body axes
x,y,z	Cartesian coordinates
$\gamma$	model-man segment Euler angle
$\eta$	fraction of frustum height at which frustum center of mass is located
$\mu$	ratio of base radii of conical frustum
$\pi = 3.14159$	
$\rho$	density, mass per unit volume
$\sigma = 1 + \mu + \mu^2$	
$\psi, \theta, \varphi$	Euler angles for spacecraft (see fig. 39)
$\Omega$	angular velocity
$\Omega_x, \Omega_y, \Omega_z$	spacecraft body rates
Subscripts:	
cal	related to calibration values

cm	related to center of mass
E	external
F	foot
H	head
HA	hand
j	jth segment of model man (j = 1, 2, . . . , 9)
LA	lower arm
LL	lower leg
LT	lower torso
M	man
MI	related to reference axes of model man
o	related to geometric spacecraft origin
RB	rigid body
S	spacecraft
T	total
UA	upper arm
UL	upper leg
UT	upper torso
$\left. \begin{array}{l} X, Y, Z \\ x, y, z \end{array} \right\}$	with respect to X-, Y-, and Z-axis
1,2,...,9	segment 1, 2, . . . , 9 of model man

Dots over symbols indicate derivatives with respect to time.

$\{\}$  denotes a vector quantity (see appendix B)

$[\ ]$  denotes a matrix (see appendix B)

## EXPERIMENT HARDWARE DEVELOPMENT

Determination of the characteristics of crew-motion disturbances, including the verification of analytical crew-motion models, requires that certain data be obtained from experiment T-013. Body-limb motion and center-of-mass translation histories must be measured simultaneously with the measurement of any forces and moments produced by the motions. During portions of the experiment, vehicle control-system response must also be measured simultaneously in order to assess its performance in the presence of known crew disturbances. The following sections will discuss the definition and development of flight hardware to meet the objectives of the Crew/Vehicle Disturbances Experiment.

### Limb-Motion Sensors

The two prime candidates for a limb-motion sensor system (hereinafter referred to as LIMS) evaluated during the definition of experiment T-013 were motion pictures and an exoskeletal device. Trade-off studies were performed to determine whether an exoskeleton or a photographic system would be more advantageous in the flight experiment limb-motion measurement. The prime advantage of motion pictures is that they permit complete freedom of body motion, although certain restrictions might be imposed on the experiment to ensure that all necessary limb segments would be in the camera's field of view. In addition, motion pictures could utilize existing onboard cameras for the limb-motion measurement function, as well as providing astronaut center-of-mass location and torso attitude data. Their outstanding disadvantages are the large amount (980 m) of film required to obtain necessary data resolution and the extensive amount of manual data reduction needed to obtain the time histories of the body-segment motions. Advantages of an exoskeleton LIMS, utilizing potentiometers at principal rotation points on the human body, are the ease of data reduction and the resultant savings in experiment weight. Its major disadvantage is that some restriction is imposed on subject motion; however, proper design and sizing of the exoskeleton could minimize its restrictions so that virtually all routine body movements could be performed in a natural manner. Table II summarizes the results of the trade-off comparison. It was concluded that the exoskeleton offers advantages over motion pictures and this concept was selected.

**TABLE II.- TRADE OFF BETWEEN EXOSKELETAL AND MOTION-PICTURE  
CONCEPTS FOR LIMB MOTION MEASUREMENTS**

	Exoskeleton	Motion pictures
Orbited weight, kg . . . . .	≈4.2	6.4
Orbited volume, m <sup>3</sup> . . . . .	≈0.11	0.02
Data reduction cost per minute of experiment time (approximate) . . . . .	<\$20	>\$800
Return weight, kg . . . . .	0	6.4
Return volume, m <sup>3</sup> . . . . .	0	0.02
Restricts body motion . . . . .	Possible	Could impose restraints for camera coverage
Measurement accuracy, degrees of limb motion . . . . .	±1.2	±3.2

A laboratory model LIMS (shown in fig. 2) was constructed and used to verify its measurement compatibility with the dynamic equations given in appendix B. Optimized design concepts for a lightweight exoskeleton LIMS were developed. These concepts included the mating of the exoskeleton to a one-piece form-fitting garment (similar to coveralls) that would provide for the maintenance of alinement between exoskeleton and body limbs and would simplify donning and doffing. This one-piece suit would be of such material and construction that a stretch capability would exist in order to allow for possible variations in experiment subject sizes. Figure 3 depicts the LIMS to be used in the flight experiment. It consists of an aluminum exoskeleton, with 16 potentiometers to measure rotations at the principal body joints (see fig. 4). Power (at 5 V d.c.) to the potentiometers and data signal return is via an electrical umbilical attached to the LIMS and the experiment data system. The exoskeleton is adjustable and can fit the entire range of astronaut sizes, while expansion panels in the one-piece suit extend its range of fit to several subject sizes. The LIMS, along with its data umbilical, is launched in a stowage container (shown in fig. 5). This container provides protection from the loads imposed during launch of the spacecraft and also affords protection from dust and debris during periods of nonuse.

#### Force Measuring System

The measurement of forces and moments produced by the T-013 subject astronaut requires apparatus similar to the six-component strain-gage balances used in many wind tunnels. However, it must be rugged enough to withstand normal handling and launch vibration loads. An array of load cells was selected as being the easiest to fabricate and



POTENTIOMETERS (2 OF 16)

L-71-7122

Figure 2.- Laboratory model of limb-motion measurement system.



L-71-7123  
Figure 3.- Flight-type astronaut limb-motion sensing system (LIMS).

maintain (with respect to a strain-gage balance, for example), as well as having the capability to survive the launch environment. Of the load-cell array configurations considered, the configuration shown schematically in figure 6 was selected. In addition to providing minimum weight and volume, this configuration provides essentially equal sensitivity about all three measurement axes. Using this arrangement, triaxial forces and moments are computed from the following relations:

$$F_x = \cos 45^\circ [F_1 - F_6 + \cos 60^\circ (F_2 - F_3 + F_4 - F_5)] + F_{x,cal}$$

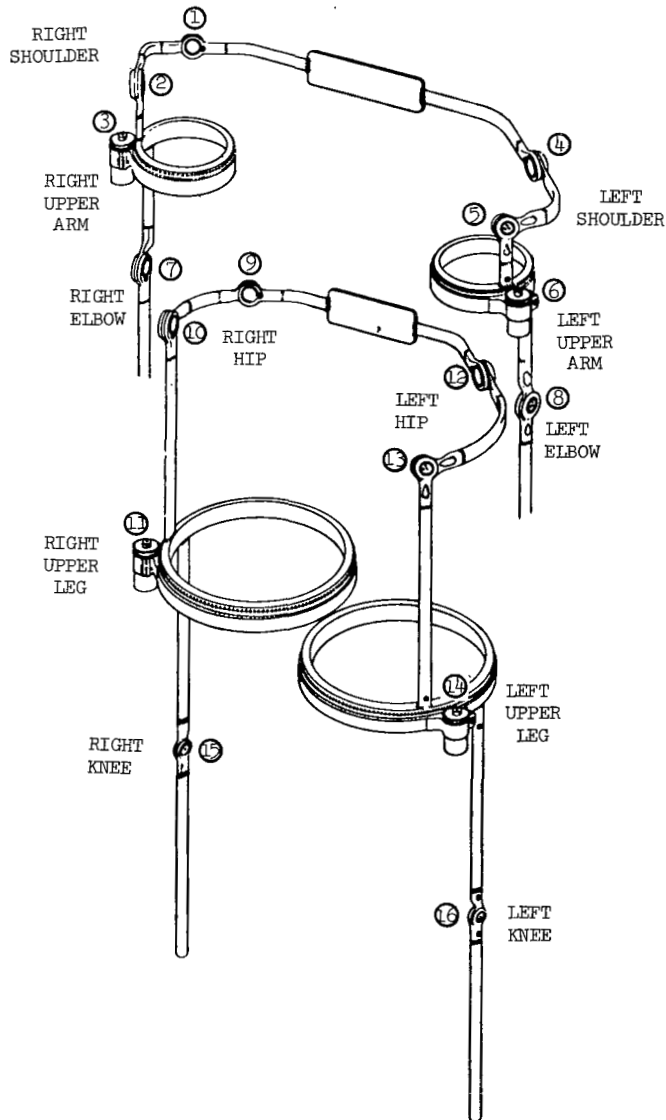


Figure 4.- LIMS exoskeleton showing potentiometer locations.

$$F_y = \cos 45^\circ \sin 60^\circ (-F_2 + F_3 + F_4 - F_5) + F_{y,cal}$$

$$F_z = \sin 45^\circ (F_1 + F_2 + F_3 + F_4 + F_5 + F_6) + F_{z,cal}$$

$$M_x = k \sin 45^\circ [-F_1 - F_6 + \cos 60^\circ (F_2 + F_3 + F_4 + F_5)] + M_{x,cal}$$

$$M_y = k \sin 45^\circ \sin 60^\circ (-F_2 - F_3 + F_4 + F_5) + M_{y,cal}$$

$$M_z = k \cos 45^\circ (F_1 - F_2 + F_3 - F_4 + F_5 - F_6) + M_{z,cal}$$

where the symbols with subscript "cal" denote terms that may arise from structural interactions of the array, and would be determined from a calibration of the load-cell array.

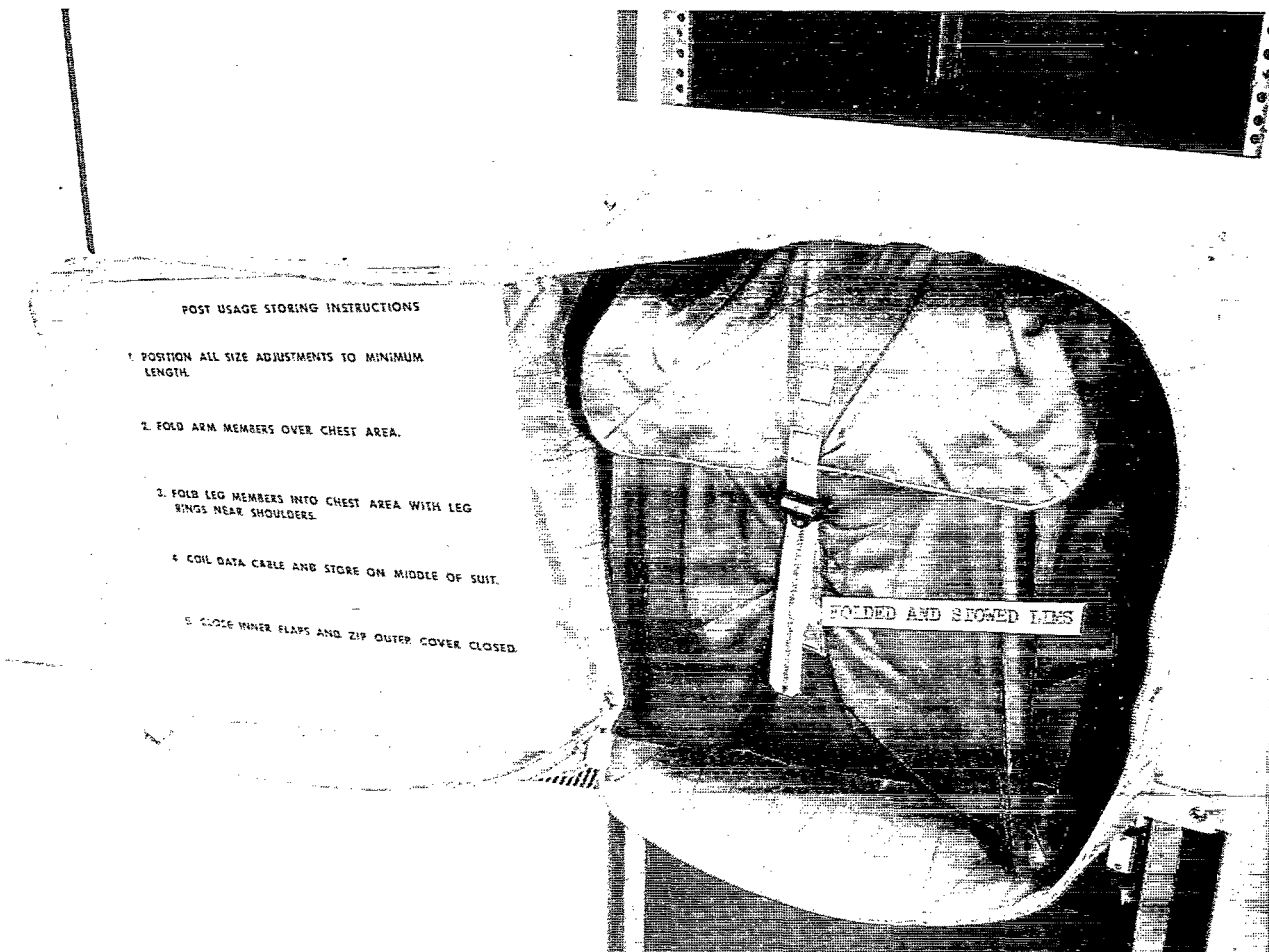


Figure 5.- Flight-type LIMS stowage container.

L-71-7124

A laboratory model of a force measurement unit (FMU) was used in simulation studies (discussed in a subsequent section) to verify measurement capability (see fig. 7). Figure 8 depicts the flight hardware FMU. Two such units will be utilized to permit investigation of the translational effects of the astronaut as he moves from one to the

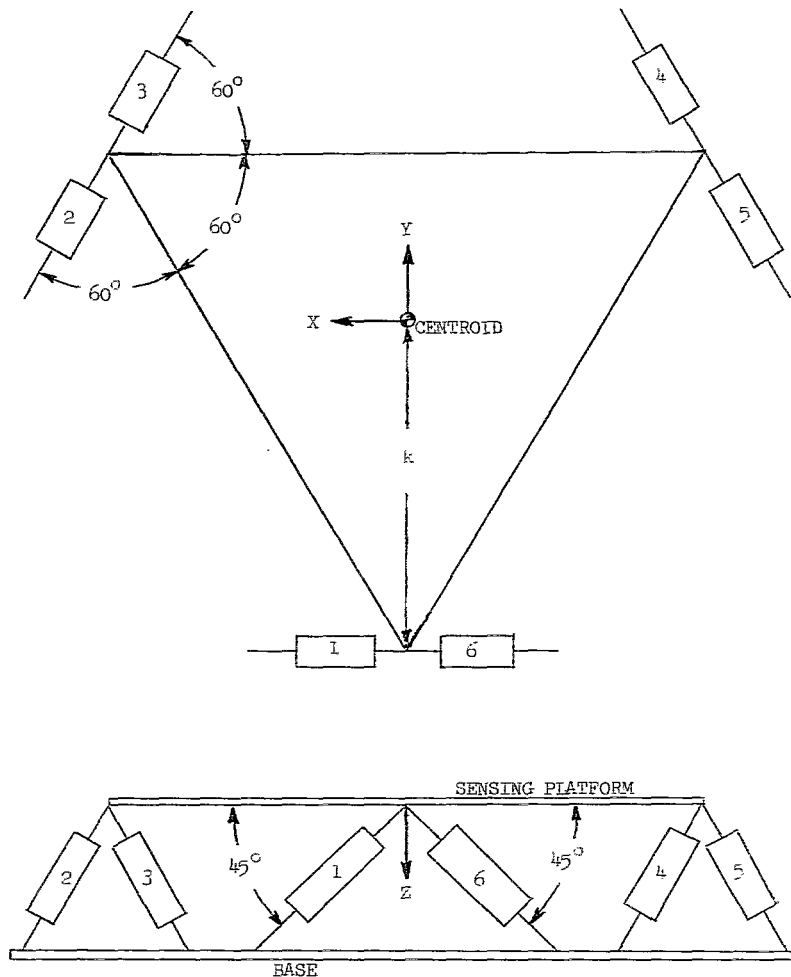
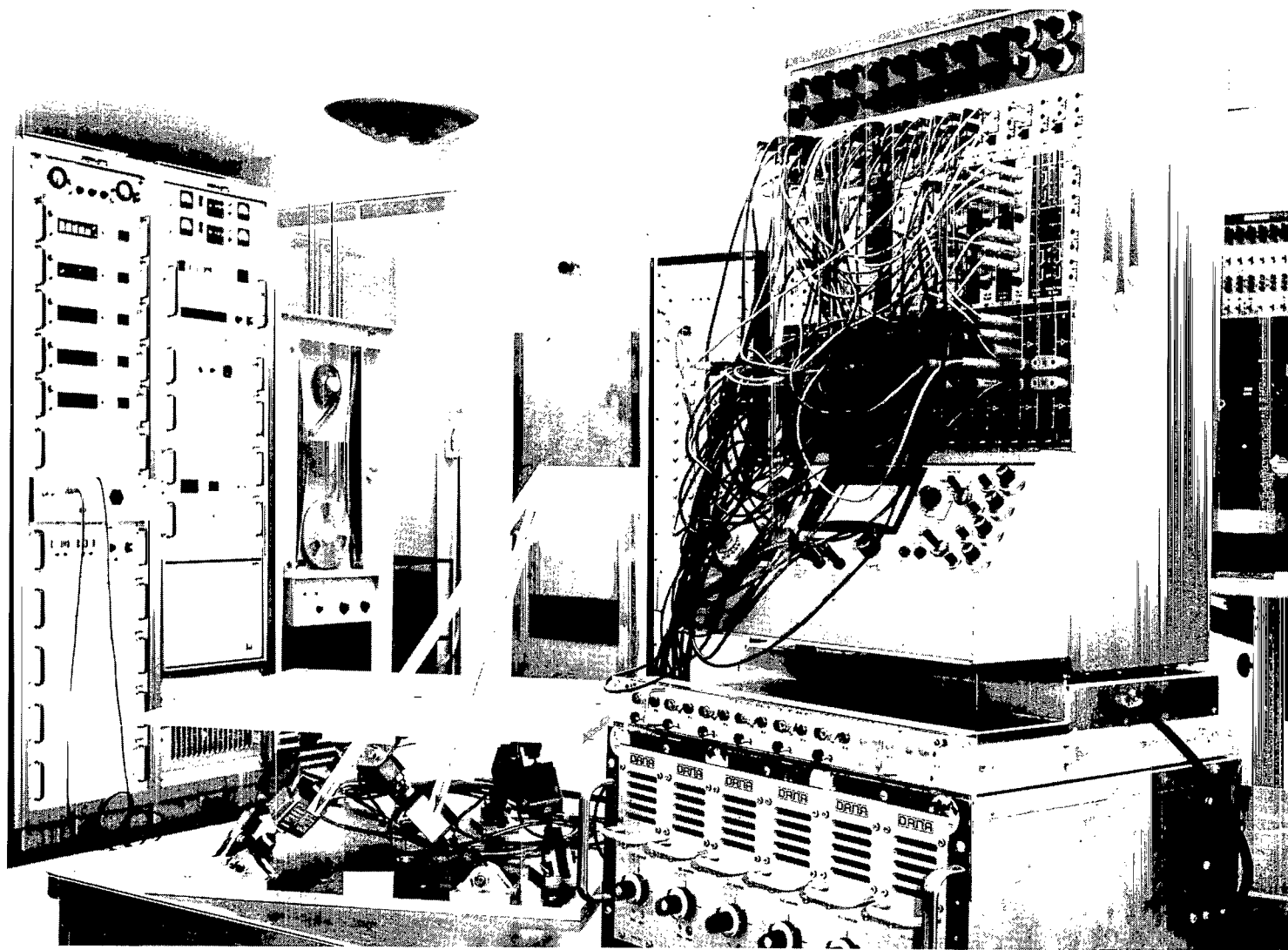


Figure 6.- Schematic drawing of load-cell configuration selected for flight hardware implementation.

other and to provide a measure of redundancy in that either could be used for evaluation of activity where the subject is attached to a single location in the spacecraft. Foot restraints (shown in fig. 8) on one FMU permit the astronaut to be restrained for studies of "restrained" or "in-place" motion effects.

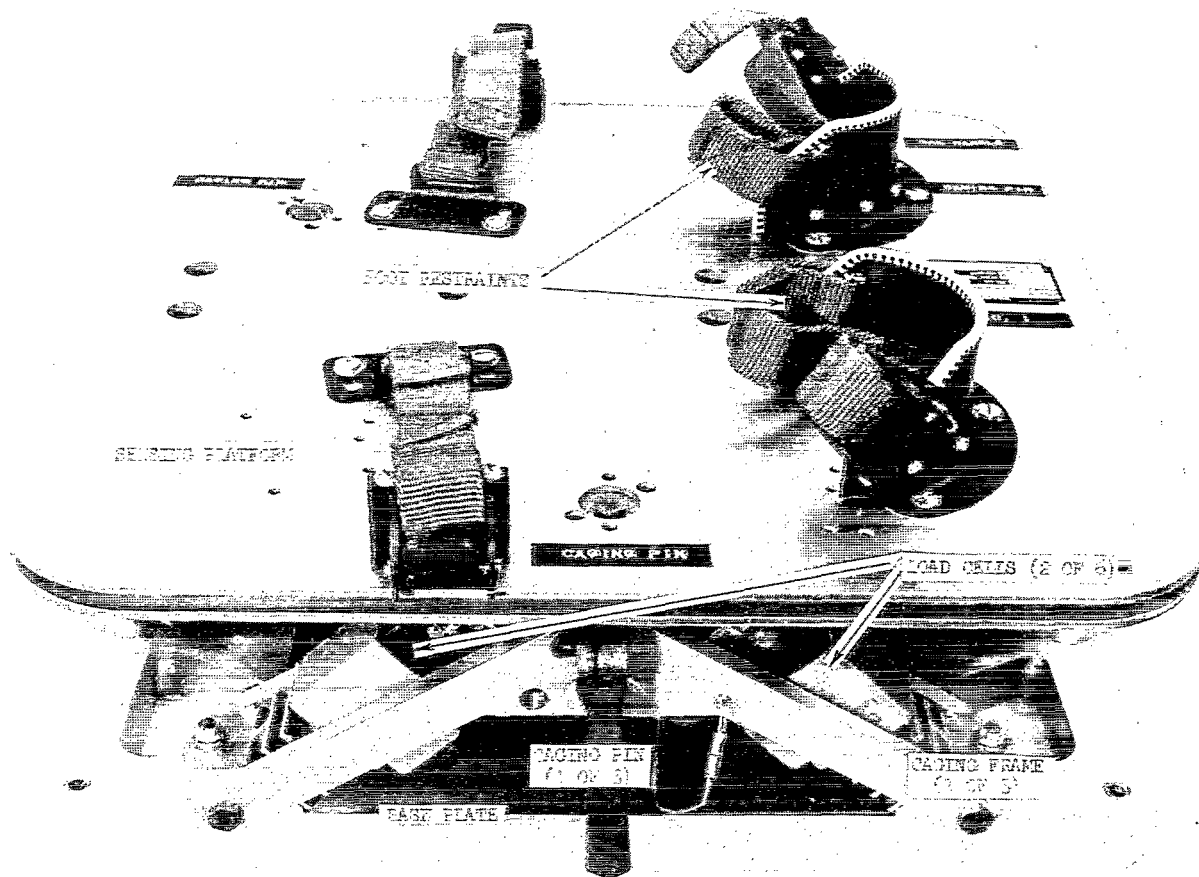
#### Astronaut Position and Attitude Determination

In order to define completely an astronaut's location and orientation within a spacecraft, histories of his center-of-mass motion and torso attitude must be known along with his limb motions, since all limb-motion measurements are referenced to the torso (or



L-71-7125

Figure 7.- Laboratory model of force measuring unit. Associated power input and data readout electronics are shown also.



L-71-7126

Figure 8.- Flight-type force measuring unit (FMU).

segment 1 of the analytical model). Several means of monitoring these histories during the performance of experiment T-013 were investigated. These methods include slow-rate motion pictures, inertial measuring unit, and ultrasonic audio signal tracking.

The motion-picture concept utilized two cameras and conventional photographic triangulation. Frame rate of the cameras was 6 frames per second, which would be adequate to obtain the necessary torso attitude and center-of-mass translation histories, since expected rates of motion for these quantities is significantly lower than rates of individual limb articulations.

The inertial-measuring-unit concept consisted of six accelerometers mounted on an orthogonal yoke worn by the astronaut. This scheme would require periodic updating (whenever acceleration levels dropped below sensor threshold, for example) and would need highly accurate transducers to be able to determine distance with the same accuracy as velocity.

The ultrasonic-triangulation method used an ultrasonic transmitter initiating a pulse simultaneously with a radio frequency (RF) transmitter, both located on the subject. The delay time between receiving the RF pulse and the ultrasonic pulse would be directly dependent on the distance from the receiver to the astronaut. This method would require multiple receivers and several transmitters in order to determine both center-of-mass location and body torso orientation. It would also require knowledge of the spacecraft atmospheric properties for determination of the speed of sound in that medium.

The photographic technique was chosen because it made use of existing onboard camera equipment, and did not entail the mechanization complexity of the other methods. Appendix G of reference 8 presents an example of a method of photogrammetry that may be used to reduce T-013 astronaut position and attitude data.

### Experiment Data System

The experiment data system is designed in such a manner that data reduction is facilitated. For T-013, measurements must include data from the LIMS and FMU's, along with a timing reference from the spacecraft central timing system. A commutator, which would sequentially sample each experiment transducer and the timing signal, was selected. The commutated data will be formatted into a single serial bit stream for input to the spacecraft tape recorders and stored for subsequent telemetry to ground receiving stations. Figure 9 shows the flight data system which features a switch to activate power to the LIMS, through the data umbilical. Table III lists the experiment measurements to be processed by the T-013 data system.

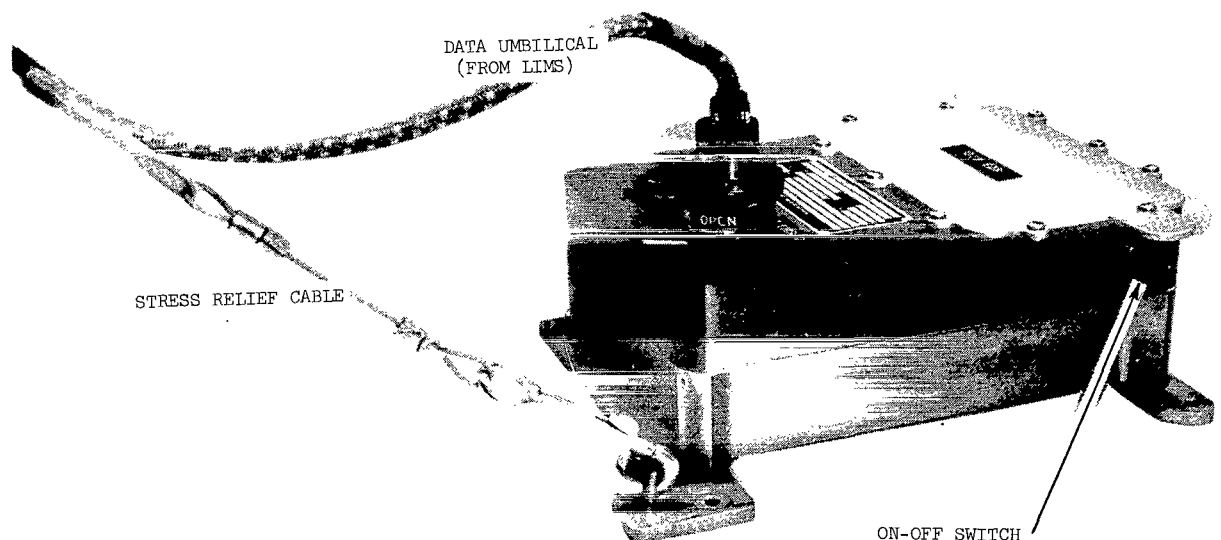


Figure 9.- Flight-type experiment data system.

L-71-7127

TABLE III.- MEASUREMENTS TO BE PROCESSED BY T-013 DATA SYSTEM

Skylab measurement number	Measurement name	Sample rate, per sec
G7017 T-013	LIMS angle, right shoulder, rear	20
G7023 T-013	LIMS angle, right shoulder, forward	20
G7024 T-013	LIMS angle, right upper arm	20
G7055 T-013	LIMS angle, left shoulder, rear	20
G7054 T-013	LIMS angle, left shoulder, forward	20
G7021 T-013	LIMS angle, left upper arm	20
G7022 T-013	LIMS angle, right elbow	20
G7057 T-013	LIMS angle, left elbow	20
G7058 T-013	LIMS angle, right hip, rear	20
G7056 T-013	LIMS angle, right hip, forward	20
G7059 T-013	LIMS angle, right thigh	20
G7060 T-013	LIMS angle, left hip, rear	20
G7061 T-013	LIMS angle, left hip forward	20
G7063 T-013	LIMS angle, left thigh	20
G7062 T-013	LIMS angle, right knee	20
G7052 T-013	LIMS angle, left knee	20
S7005 T-013	FMU #1, load cell 1	20
S7004 T-013	FMU #1, load cell 2	20
S7003 T-013	FMU #1, load cell 3	20
S7007 T-013	FMU #1, load cell 4	20
S7006 T-013	FMU #1, load cell 5	20
S7009 T-013	FMU #1, load cell 6	20
S7008 T-013	FMU #2, load cell 1	20
S7001 T-013	FMU #2, load cell 2	20
S7000 T-013	FMU #2, load cell 3	20
S7011 T-013	FMU #2, load cell 4	20
S7010 T-013	FMU #2, load cell 5	20
S7002 T-013	FMU #2, load cell 6	20
M7075 T-013	FMU #1, calibration voltage	10
M7076 T-013	FMU #2, calibration voltage	10
M7077 T-013	LIMS, calibration voltage	10
K7328 T-013	Airlock module timing reference	10
K7329 T-013	T-013 identification word	10

## Spacecraft Pointing Control System

An important adjunct to the Crew/Vehicle Disturbances Experiment is the evaluation of spacecraft-control-system response to known crew-motion-disturbance inputs. Data from the Apollo telescope mount (ATM) pointing control system (described in ref. 9) will be obtained during the performance of experiment T-013 and will include control-moment gyro (CMG) gimbal angle and rate measurements, rate gyro measurements, sun sensor signals, and control-moment gyro command parameters. A complete list of ATM measurements to be obtained is found in table IV. This data will be subsequently time-

TABLE IV.- ATM MEASUREMENTS TO BE OBTAINED DURING EXPERIMENT T-013

Skylab measurement number	Measurement name	Sample rate, per sec
K122	ATM mission elapsed time	10
R017-702	CMG #1, outer gimbal rate	12
R018-702	CMG #2, outer gimbal rate	12
R019-702	CMG #3, outer gimbal rate	12
R020-702	CMG #1, inner gimbal rate	12
R021-702	CMG #2, inner gimbal rate	12
R022-702	CMG #3, inner gimbal rate	12
M164-702	Fine sun sensor, yaw output voltage	12
M165-702	Fine sun sensor, pitch output voltage	12
R023-702	Vehicle rate gyro No. 1, X-axis output	12
R024-702	Vehicle rate gyro No. 1, Y-axis output	12
R025-702	Vehicle rate gyro No. 1, Z-axis output	12
R026-702	Vehicle rate gyro No. 2, X-axis output	12
R027-702	Vehicle rate gyro No. 2, Y-axis output	12
R028-702	Vehicle rate gyro No. 2, Z-axis output	12
R029-702	Vehicle rate gyro No. 3, X-axis output	12
R030-702	Vehicle rate gyro No. 3, Y-axis output	12
R031-702	Vehicle rate gyro No. 3, Z-axis output	12
G023-702	CMG #1, inner gimbal angle	12
G024-702	CMG #1, outer gimbal angle	12
G025-702	CMG #2, inner gimbal angle	12
G026-702	CMG #2, outer gimbal angle	12
G027-702	CMG #3, inner gimbal angle	12
G028-702	CMG #3, outer gimbal angle	12
R015-702	Experiment pointing system pitch rate gyro command	12
R016-702	Experiment pointing system yaw rate gyro command	12
M529-702	Acquisition sun sensor, X output voltage, primary	12
M530-702	Acquisition sun sensor, X output voltage, redundant	12
M531-702	Acquisition sun sensor, Y output voltage, primary	12
M532-702	Acquisition sun sensor, Y output voltage, redundant	12
G037-702	Star tracker, outer gimbal angle	12
G038-702	Star tracker, inner gimbal angle	12
K382-702	Experiment pointing control system resolver output (pitch and yaw)	1.25

correlated with the FMU and LIMS data. The measurements listed in table IV will be telemetered in real-time while the orbital workshop (OWS) is over ground receiving stations, since available ATM data recorders record at a rate too low for adequate data resolution, and do not have the capability to record all measurements listed in table IV.

### EXPERIMENT DESCRIPTION

Experiment T-013 will be performed in the forward area of the Skylab orbital workshop. Figure 10 depicts the layout of this section of the spacecraft, and shows the location of the various pieces of T-013 experiment hardware (including camera placements).

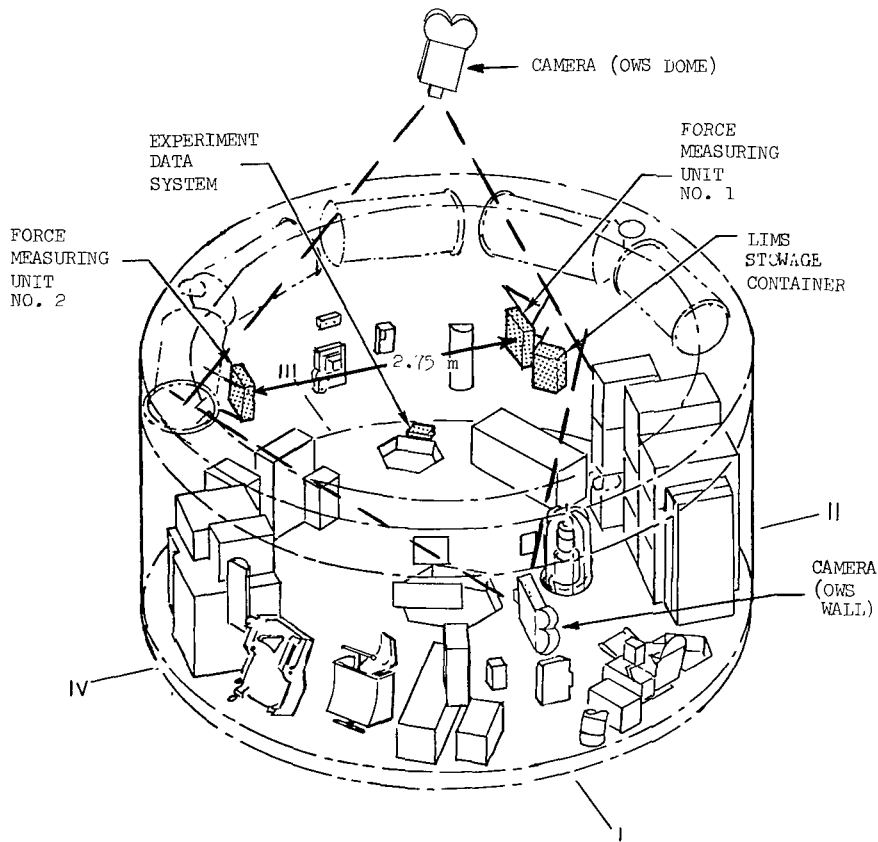


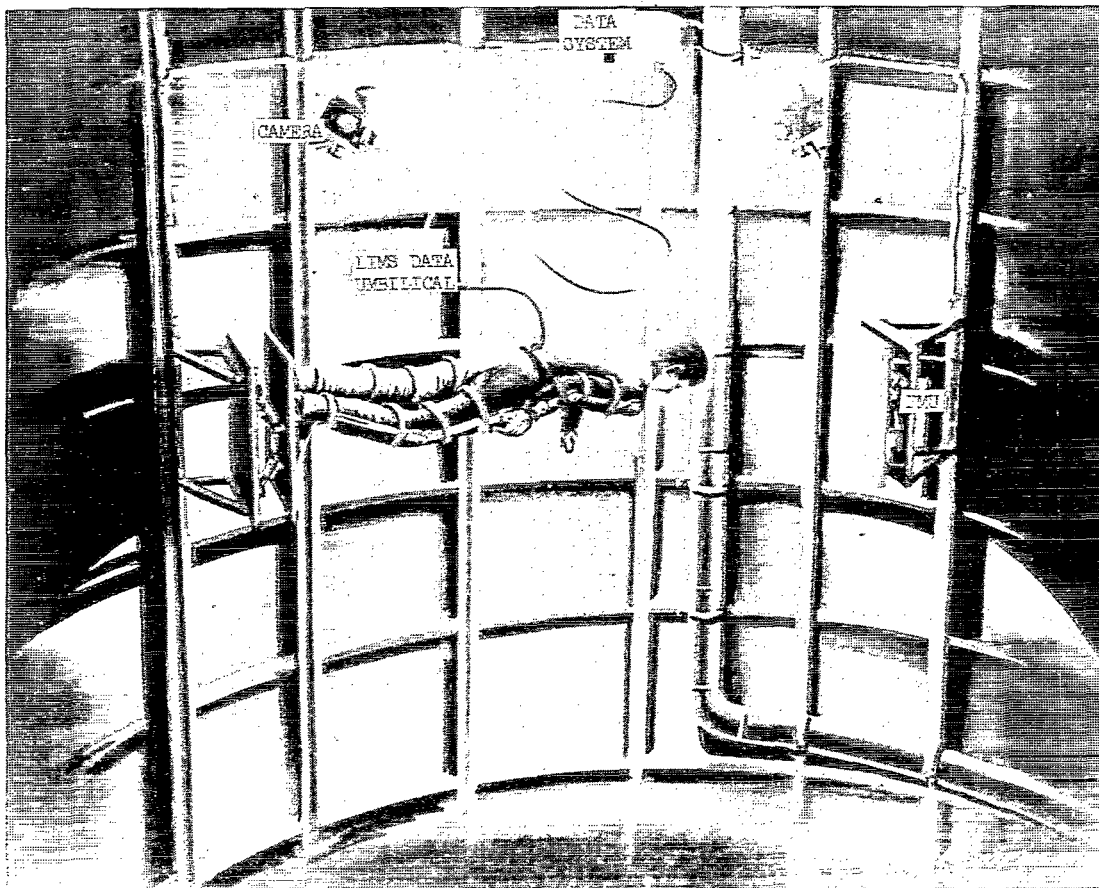
Figure 10.- Sketch of Skylab spacecraft interior showing locations of T-013 experiment hardware.

As noted on this figure, the two force measuring units are approximately 2.75 meters apart, with their sensing plates parallel, and are attached to the OWS wall structure via permanently installed brackets.

The orbital assembly (which includes the orbital workshop and the docked Apollo command-service module) will be in a nominal 435-km circular orbit, with an orbit inclination of  $50^{\circ}$ . The orbital assembly will be attitude-stabilized in the solar inertial

mode during T-013. This mode provides for keeping the Apollo telescope mount pointed toward the sun, with the long axis of the orbital workshop maintained in the orbit plane. The control moment gyros of the ATM pointing control system (PCS) will provide the primary means for spacecraft stabilization.

The T-013 subject will perform a variety of motions during the Crew/Vehicle Disturbances Experiment. These will be restricted as far as possible to motions of the 9-segment body described in the appendixes. One set of motions will be conducted while attached to one FMU; these motions include simple arm and leg pendulum-type movements, random reaching and twisting movements, and exaggerated breathing, coughing and "sneezing" functions. Figure 11 shows an artist's concept of this phase of the Skylab experiment. Free soaring translation between the FMU's, with push-offs by either hands or feet, will comprise the remainder of the experiment activity. Certain atypical motions will be performed by the subject alone and, concurrently, with a second astronaut, in order to provide a "worst-case" crew-disturbance input to the Skylab pointing control system. These motions will consist of vigorous limb movements and rapid soaring translations.



L-71-7128

Figure 11.- Artist's concept of T-013 experiment setup.

Most of the discrete motions will be performed three times by the subject, and the discrete-motion sequence will be repeated (for a total of six performances per motion) to give a degree of statistical confidence to the resultant data. The experiment performance timeline is summarized as figure 12.

An observer astronaut will assist the subject in donning and doffing the LIMS and in attaching him to an FMU. This observer will enter voice comments into the tape recorder during experiment progress; these comments will include task identification

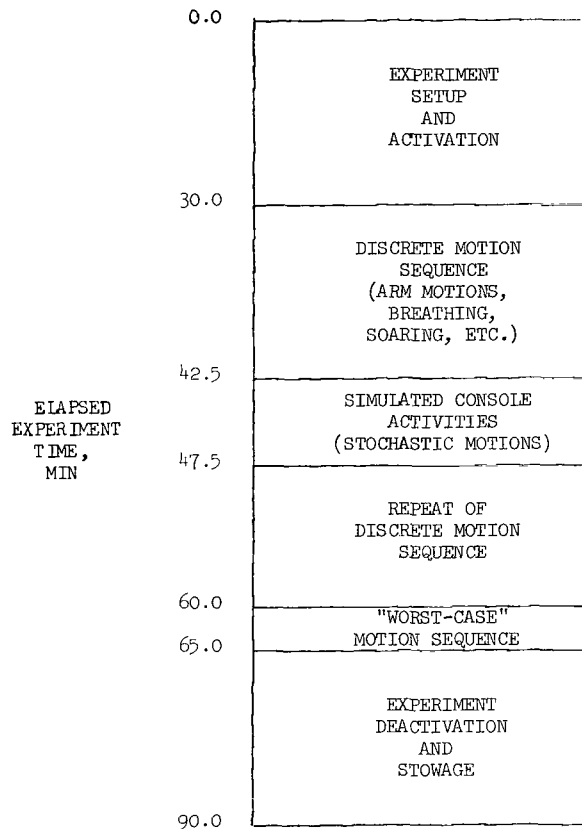


Figure 12.- T-013 experiment timeline summary.

and relayed assessments by the subject as to difficulty in performing a given task or other operational peculiarities. Another responsibility of the observer will be to actuate the data cameras and tape recorder.

Scheduling of the experiment during the Skylab flight will depend in part on available ground tracking station coverage for the "worst-case" motion sequence and other portions of T-013. Typical telemetry coverage during a given station overpass is approximately 5 minutes. Figure 13 shows the ground tracks of three representative Skylab orbits that could be used for T-013.

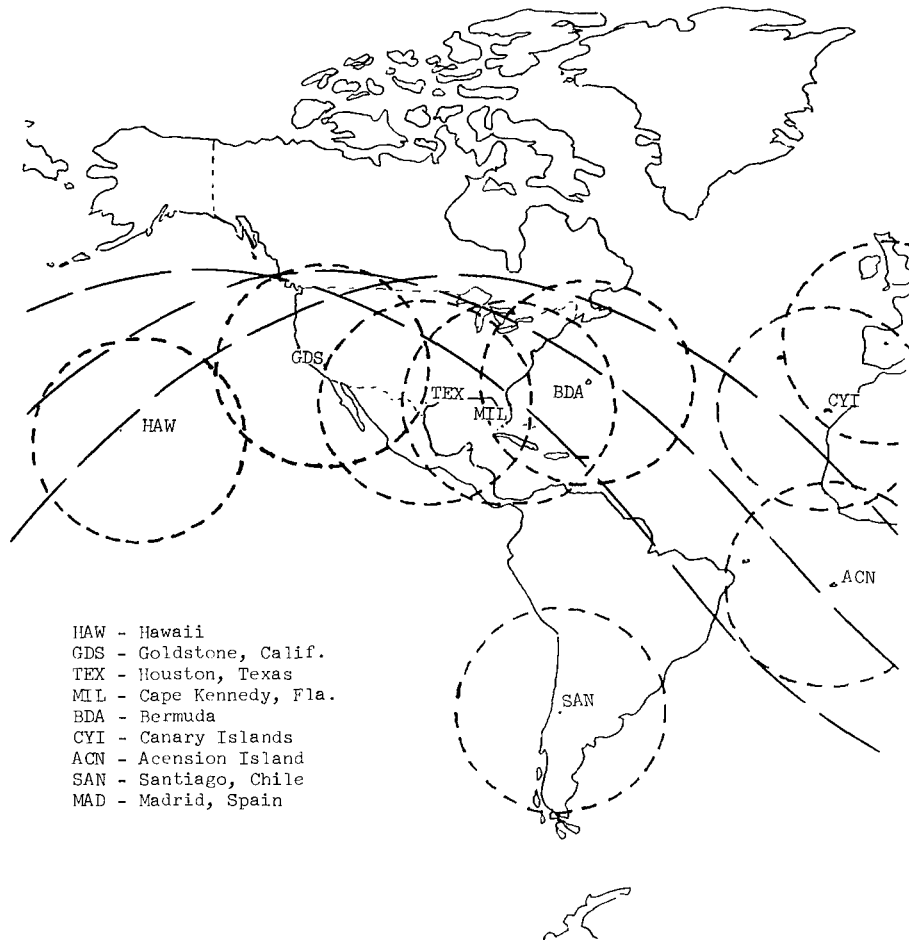


Figure 13.- Skylab western hemisphere telemetry receiving station coverage, showing ground tracks of three representative Skylab orbits.

### CREW-MOTION DATA USE AND APPLICATIONS

The data obtained from the Skylab Crew/Vehicle Disturbances Experiment will be used in the sizing, design, analysis, and simulation of control-system concepts and configurations for future manned space vehicles. Previous simulations of crew-motion disturbances have been conducted. One simulation (ref. 10) utilized a three-degree-of-freedom cable suspension scheme, with forces and moments measured by a strain-gage balance. Agreement between results of this simulation and predicted results using the analytical model of appendix B was poor. A second simulation (ref. 11) used a servo-drive six-degree-of-freedom simulator, and load-cell arrays similar to those for the T-013 flight hardware. Results of this simulation when compared to the mathematical model prediction (ref. 8) were in much closer agreement than the cable suspension results,

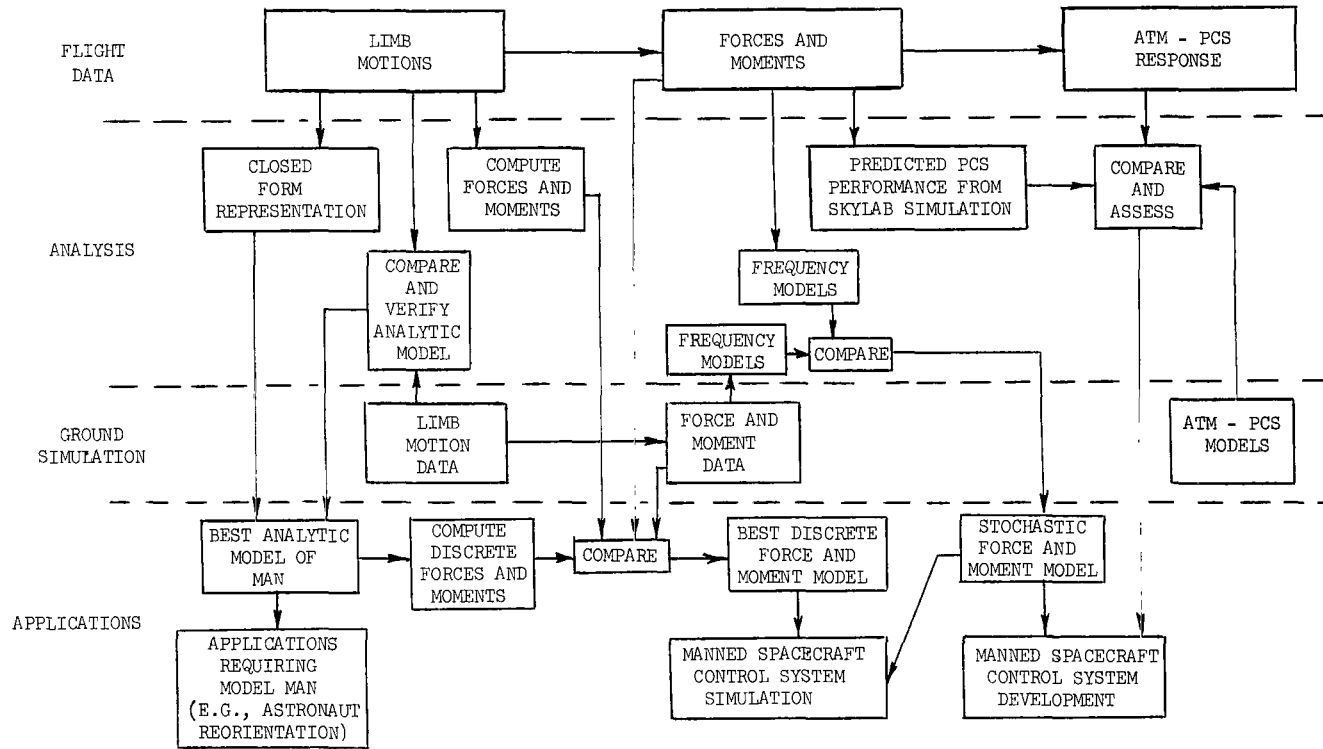


Figure 14.- Skylab experiment T-013 data use and applications.

although significant differences did exist. Variations in force and moment levels between experiment and theory are attributed to 1-g effects of the simulations, as pointed out in table I. It is expected that reduction of the data from T-013 will, in addition to providing verification of the analytical crew-motion model, permit the derivation of correction factors which can be applied to 1-g simulations to approximate more closely zero-g crew-disturbance effects. The verified analytical model may be applied to investigation of man-motion effects, with respect to astronaut maneuvering units, work capability and task analysis, and optimized reorientation maneuvers of a free-floating astronaut, for example. Crew-disturbance data from T-013 will also provide a base for developing stochastic models of crew-motion disturbances, which may be applicable to the analysis and simulation of multicrew, long-term flight activities (as initiated in ref. 7, for example). Data from the ATM PCS will provide additional verification of the dynamic model derived in appendix B. These data will also aid in evaluating the effectiveness of the Skylab control system in compensating for crew disturbances and in providing high-accuracy pointing levels for a manned spacecraft and experiment modules. A flow diagram depicting the use and applications of T-013 flight experiment data is given as figure 14.

#### CONCLUDING REMARKS

This report summarizes the development of a manned space flight experiment to investigate the characteristics of crew-motion disturbances on a manned spacecraft. The data expected from this experiment will be used in the development of attitude control systems for long-term manned space flight. An analytical crew-motion model, derived in the appendixes, may also be applied to the analysis of other man-motion phenomena and effects. Specific examples of potential applications include the use of selected limb movements to reorient a free-floating astronaut, the modeling of astronaut personnel vehicles (such as backpack maneuvering units), and work capability or task analysis (in conjunction with metabolic or energy expenditure). Verification of this mathematical model through the Skylab Crew/Vehicle Disturbances Experiment should result in a valuable tool for research into a wide variety of manned space activities.

Langley Research Center,  
National Aeronautics and Space Administration,  
Hampton, Va., November 23, 1971.

## APPENDIX A

### SEGMENT MASSES, CENTERS OF MASS, AND LOCAL MOMENTS OF INERTIA FOR AN ANTHROPOMETRIC MODEL OF MAN

By Charles T. Woolley  
Langley Research Center

The derivation of a mathematical model of the human body, by which segment inertial properties and other biomechanical data can be computed is presented in this appendix. Figure 15 depicts a frontal view of the location of several principal skeletal anthropometric points used in the model derivation, along with locations of the body reference planes. A lateral view of the remaining anthropometric point and the body reference planes is shown in figure 16.

An orthogonal coordinate system is used as a body reference system. This system is defined by the intersection of the three principal body planes shown in figures 15 and 16. The  $X_{MI}$ -axis is formed by the intersection of the sagittal and transverse planes, with  $+X_{MI}$  directed toward the front of the body; the  $Y_{MI}$ -axis is defined by the intersection of the frontal and transverse planes, with  $+Y_{MI}$  directed toward the right side of the body; the  $Z_{MI}$ -axis is defined by the intersection of the sagittal and frontal planes, with  $+Z_{MI}$  directed toward the feet to complete the right-handed axis system. The origin of the coordinate system is located at the intersection of the three body reference planes as shown in figures 15 and 16.

Figure 17 illustrates the relation of the body segments. Segment 1 is treated as a rigid member and results from the combination of three solids: the head is represented by an ellipsoid, and the upper and lower torso are represented by right elliptic cylinders. A lower arm segment (segments 4 and 5) is a combination of a sphere for the hand and a frustum of a right circular cone for the lower arm. Another compound segment is the lower leg (segments 8 and 9); this segment is a combination of two frusta of cones, one representing the lower leg, and another representing the foot. All other body parts are approximated by simple frusta of right circular cones.

To use the mathematical model in crew-motion simulations, the relative locations of the segment centers of mass and the segment hinge points must be specified. Figure 18 shows these locations, along with orientation of the coordinate axes.

The model of the human body described in this appendix is a modification and extension of a 15-segment model developed by Hanavan (ref. 5). The current development reduces the number of segments to nine by the combination described above. It is recognized that the nine-segment model possesses possible limitations in use for crew-motion-

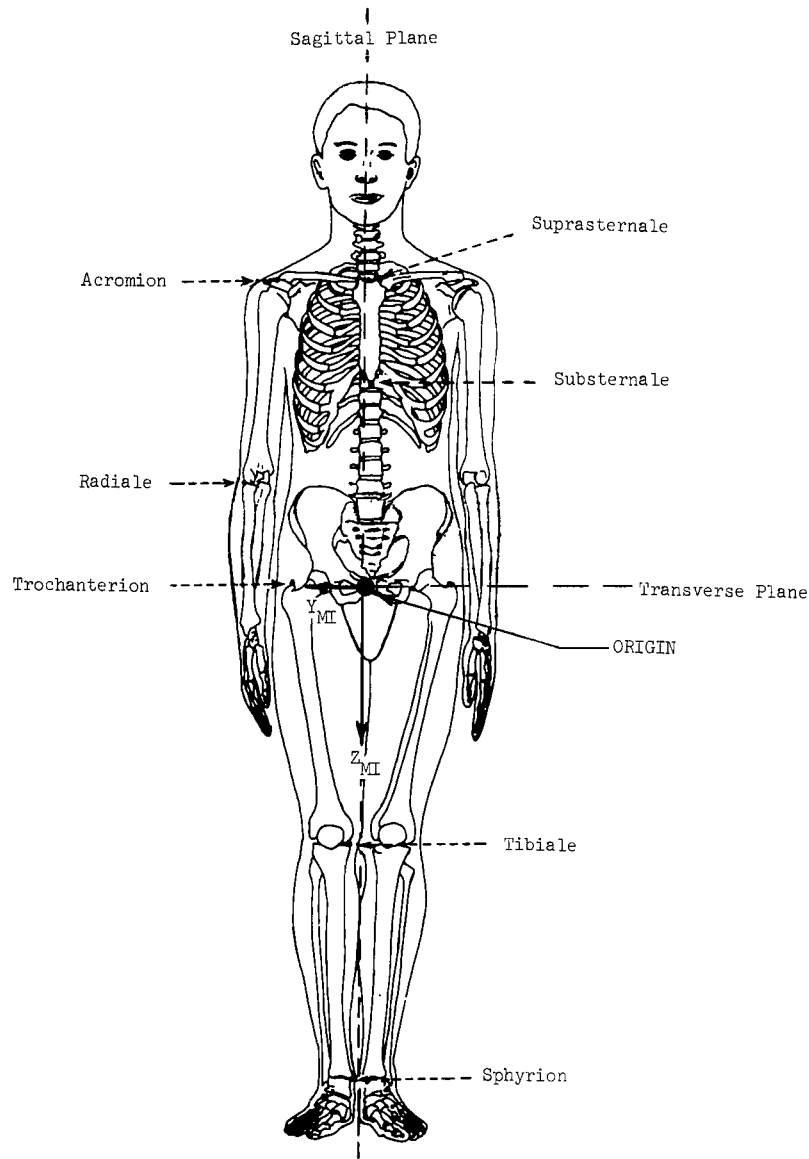


Figure 15.- Frontal view of human skeleton, showing location of body-reference planes and principal anthropometric points used in derivation of analytical model.

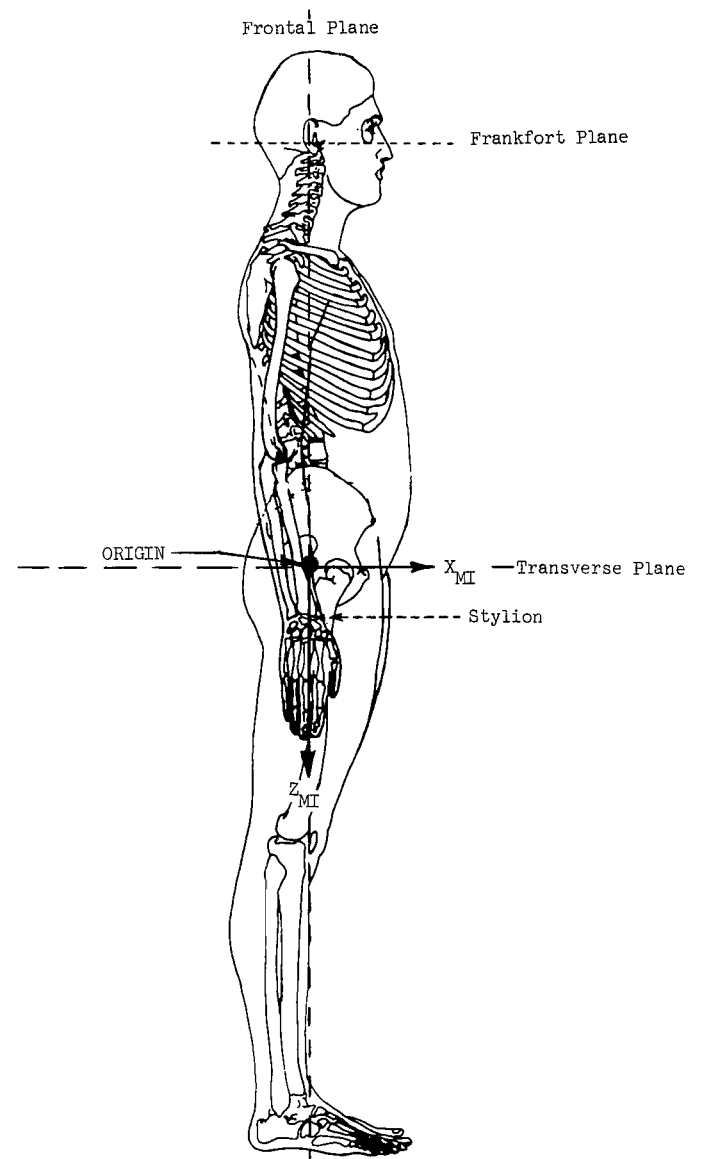


Figure 16.- Lateral view of human skeleton, showing location of one anthropometric point and the body reference planes.

APPENDIX A - Continued

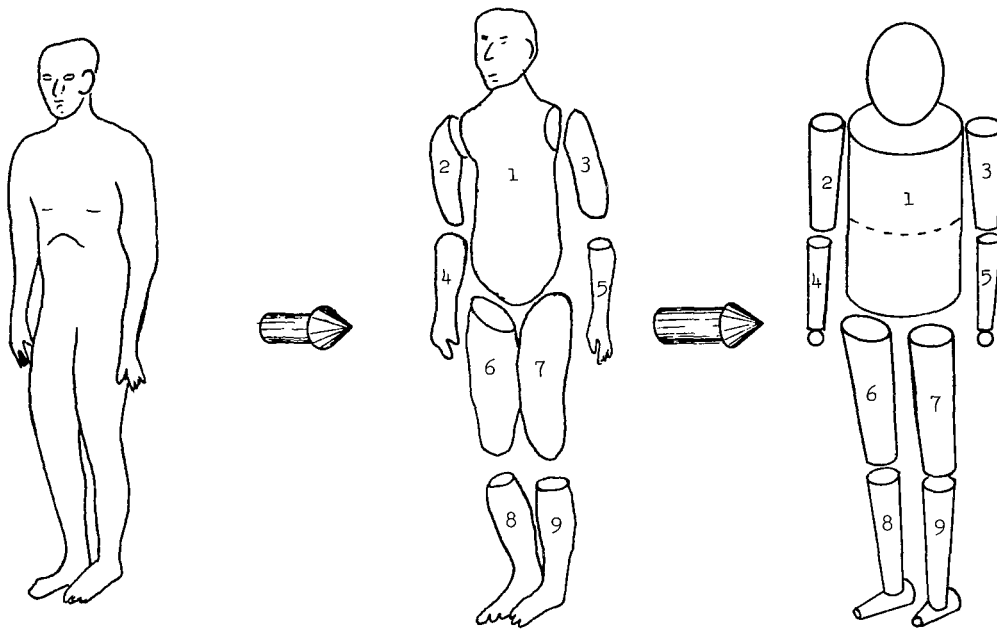


Figure 17.- Nine-segment model of man.

disturbance analyses. No account is taken of wrist, ankle, or head motions, nor of bending of the spine. However, the hands and feet are relatively small masses when compared to other body segments, and would provide minimal disturbance effects if moved vigorously; whereas, the head and spinal motions involve larger masses which could affect T-013 experiment data. The T-013 motion sequences will be constrained to movements (insofar as possible) of only the nine principal segments.

Twenty-four standard anthropometric measurements are used to dimension the model segments. Table V contains a list of these measurements, their abbreviations which will be used in the development to follow, and brief descriptions of the measurements. Complete descriptions of the measurements are found in reference 4.

The man's total body mass must be distributed over each of the body segments. Barter (ref. 6) devised a set of regression equations which will be used for the distribution process. These regression equations are given below:

Mass of:

$$\text{Head, neck, and trunk} \equiv \text{HNT} = 0.47m'_T + 5.44 \text{ kg}$$

$$\text{Both upper arms} \equiv \text{BUA} = 0.08m'_T - 1.32 \text{ kg}$$

$$\text{Both forearms} \equiv \text{BFO} = 0.04m'_T - 0.23 \text{ kg}$$

$$\text{Both hands} \equiv \text{BH} = 0.01m'_T + 0.32 \text{ kg}$$

APPENDIX A - Continued

Both upper legs  $\equiv$  BUL  $= 0.18m'_T + 1.45$  kg

Both lower legs  $\equiv$  BLL  $= 0.11m'_T - 0.86$  kg

Both feet  $\equiv$  BF  $= 0.02m'_T + 0.68$  kg

where

$$m'_T = \frac{m_T - 5.48}{0.91}$$

The corrected total mass of model man  $m'_T$  distributes mass proportionately to the segment masses.

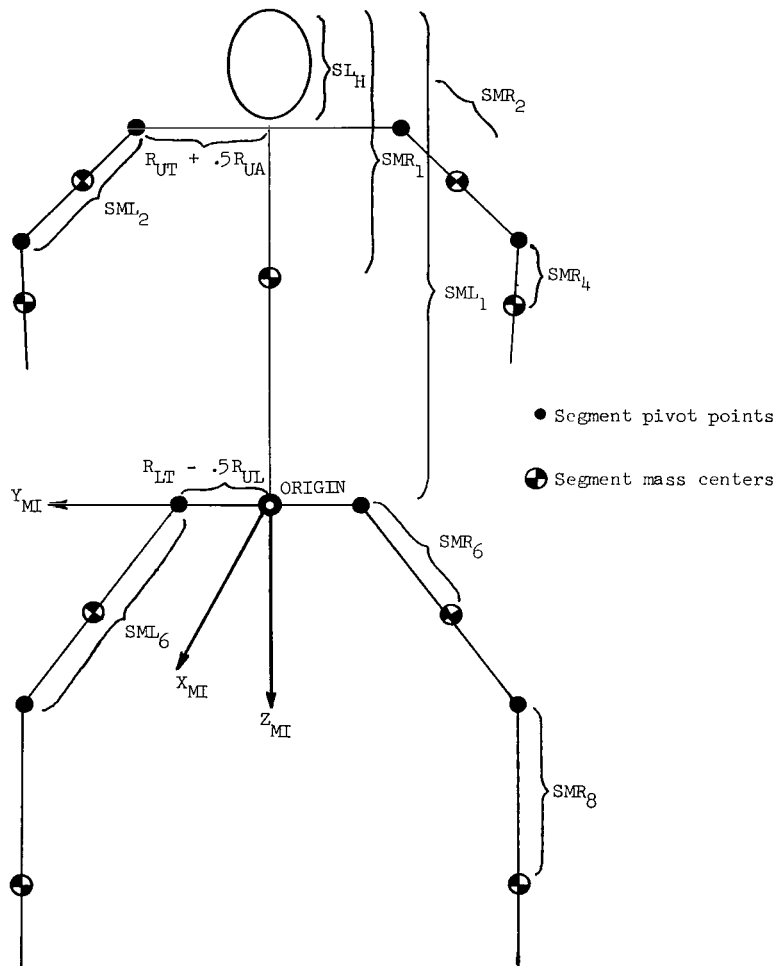


Figure 18.- Locations of segment hinge points and centers of mass and coordinate axis orientation.

TABLE V.- ANTHROPOMETRIC MEASUREMENTS

Measurement	Abbreviation	Brief description
Ankle circumference	ANKC	Minimum circumference of right ankle
Axillary arm circumference	AXILC	Horizontal circumference of upper arm at armpit
Buttock depth	BUTTD	Front-to-rear dimension of body at buttocks
Chest breadth	CHESB	Width of body (less arms) at level of nipples
Chest depth	CHESD	Front-to-rear dimension of chest at level of nipples
Elbow circumference	ELBC	Circumference of arm at elbow (arms extended)
Fist circumference	FISTC	Circumference of fist measured over thumb and knuckles
Forearm length	FOARL	Length of extended lower arm between elbow and wrist
Foot length	FOOTL	Maximum length of foot from heel to toe
Knee circumference	GKNEC	Circumference of right knee at kneecap (standing)
Head circumference	HEADC	Maximum circumference of head above eyebrows
Hip breadth	HIPB	Maximum width of body at hips
Shoulder (acromial) height	SHLDH	Distance from floor to right shoulder (acromion), standing
Sitting height	SITH	Height from seat to top of head, subject sitting erect with knees bent 90°
Sphyrion height	SPHYH	Distance from floor to sphyrion (ankle), subject standing
Stature	STAT	Distance from floor to top of head, subject standing erect
Substernale height	SUBH	Distance from floor to substernale (lower breastbone), subject standing
Thigh circumference	THIHC	Horizontal circumference of upper right thigh, standing
Tibiale height	TIBH	Distance from floor to tibiale (knee), subject standing
Trochanteric height	TROCH	Distance from floor to trochanterion (hip), subject standing
Upper arm length	UPARL	Distance from acromion to radiale (shoulder to elbow), arm at side
Waist breadth	WAISB	Minimum width of waist, standing
Waist depth	WAISD	Front-to-rear dimension of body at waist
Wrist circumference	WRISC	Minimum circumference of wrist, arm extended

## APPENDIX A - Continued

### Segment Development

The following section will develop the properties of the nine body segments. Each segment will be assigned a coordinate axis system, with its origin at the segment center of mass. Orientation of each coordinate system will be such that the segment X-, Y-, and Z-axis will be parallel to the  $X_{MI}$ -,  $Y_{MI}$ -, and  $Z_{MI}$ -axis, respectively, when the body is in a normal standing position, with arms hanging vertically by the sides. The segment properties development follows that of Hanavan in reference 5.

Head and torso (segment 1).- As shown in figure 19, the head of the model man is represented by a right circular ellipsoid. The segment is oriented so as to produce a

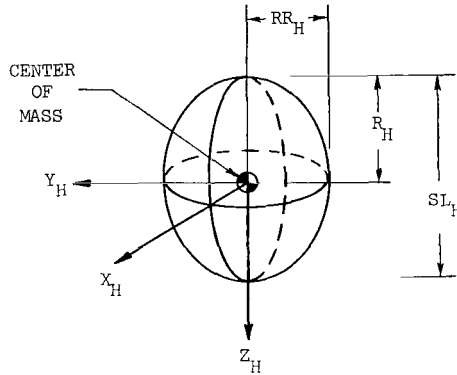


Figure 19.- Head of model man (right circular ellipsoid).

circular cross section in a plane parallel to the transverse plane. The dimensions and properties of the head are given by

$$\left. \begin{aligned}
 R_H &= 0.5(\text{STAT} - \text{SHLDH}) \\
 RR_H &= \text{HEADC}/2\pi \\
 SL_H &= \text{STAT} - \text{SHLDH} = 2R_H \\
 R_H &= 0.5SL_H \\
 V_H &= 4\pi R_H \cdot (RR_H)^2/3 \\
 m_H &= 0.079m_T \quad (\text{from Dempster, ref. 3}) \\
 \rho_H &= m_H/V_H \\
 SI_{XX,H} &= 0.2m_H \left[ (R_H)^2 + (RR_H)^2 \right] \\
 SI_{YY,H} &= SI_{XX,H} \\
 SI_{ZZ,H} &= 0.4m_H \cdot (RR_H)^2
 \end{aligned} \right\} \quad (A1)$$

Right elliptical cylinders are used to simulate both the upper and lower torso. The orientation is such as to produce elliptical cross sections in planes parallel to the transverse plane.

APPENDIX A - Continued

The mass of the entire torso is found by subtracting the mass of the head from the mass of the head, neck, and trunk. A ratio of the densities is then used to find the mass of each of the upper and lower torsos.

The upper torso is shown in figure 20. The dimensions and properties of the upper torso are given by

$$\begin{aligned}
 R_{UT} &= 0.5CHESB \\
 RR_{UT} &= 0.25(CHESD + WAISD) \\
 SL_{UT} &= SHLDH - SUBH \\
 SR_{UT} &= 0.5SL_{UT} \\
 V_{UT} &= \pi \cdot R_{UT} \cdot RR_{UT} \cdot SL_{UT} \\
 V_{LT} &= \pi \cdot R_{LT} \cdot RR_{LT} \cdot SL_{LT} \\
 \rho_{UT} &= (HNT - m_H) / (V_{UT} + rV_{LT})
 \end{aligned}$$

where

$$r = \frac{\text{Specific gravity}_{LT}}{\text{Specific gravity}_{UT}} = \frac{1.01}{0.92} \quad (\text{from Dempster, ref. 3})$$

(A2)

$$m_{UT} = \rho_{UT} \cdot V_{UT}$$

$$SI_{XX,UT} = m_{UT} \left[ 3(R_{UT})^2 + (SL_{UT})^2 \right] / 12$$

$$SI_{YY,UT} = m_{UT} \left[ 3(RR_{UT})^2 + (SL_{UT})^2 \right] / 12$$

$$SI_{ZZ,UT} = m_{UT} \left[ (R_{UT})^2 + (RR_{UT})^2 \right] / 4$$

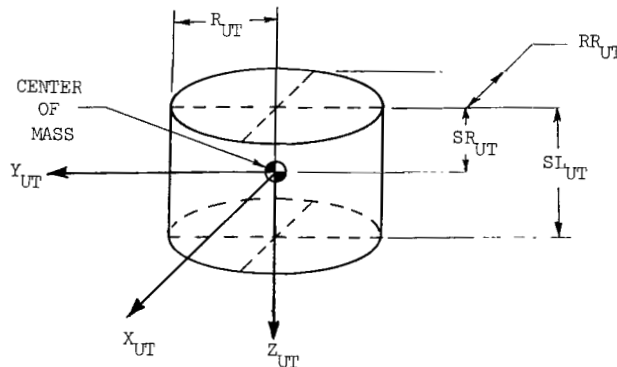


Figure 20.- Right elliptic cylinder representing the upper torso of model man.

APPENDIX A - Continued

Figure 21 shows the lower torso of the model. The dimensions and properties of the lower torso are given by

$$\left. \begin{aligned}
 R_{LT} &= 0.5HIPB \\
 RR_{LT} &= 0.25(WAISD + BUTTD) \\
 SL_{LT} &= SITH - (STAT - SUBH) \\
 SR_{LT} &= 0.5SL_{LT} \\
 V_{LT} &= \pi \cdot R_{LT} \cdot RR_{LT} \cdot SL_{LT} \\
 m_{LT} &= HNT - m_H - m_{UT} \\
 \rho_{LT} &= m_{LT}/V_{LT} \\
 SI_{XX,LT} &= m_{LT} \left[ 3(R_{LT})^2 + (SL_{LT})^2 \right] / 12 \\
 SI_{YY,LT} &= m_{LT} \left[ 3(RR_{LT})^2 + (SL_{LT})^2 \right] / 12 \\
 SI_{ZZ,LT} &= m_{LT} \left[ (R_{LT})^2 + (RR_{LT})^2 \right] / 4
 \end{aligned} \right\} \quad (A3)$$

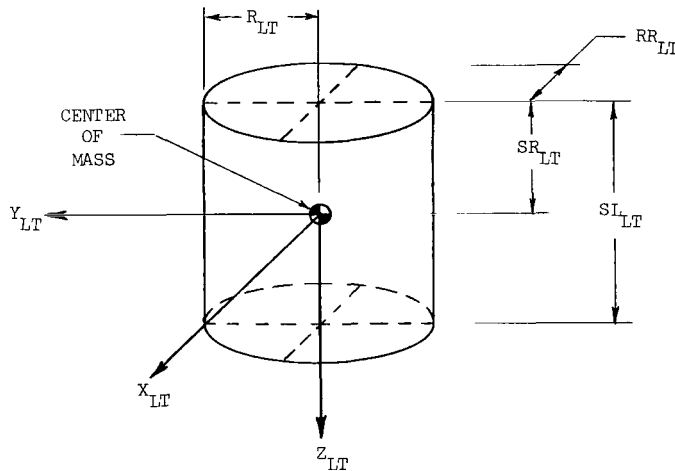


Figure 21.- Right elliptic cylinder representing the lower torso of model man.

These first three solids are combined to form the first segment of the model man. The resultant segment is shown in figure 22. The dimensions and properties of the total torso segment are given by

APPENDIX A - Continued

$$\left. \begin{aligned}
 \text{DELSH} &= \text{SITH} - \text{STAT} - \text{TROCH} \\
 \text{SL}_1 &= \text{SL}_H + \text{SL}_{UT} + \text{SL}_{LT} \\
 \text{SML}_1 &= \text{SL}_1 - \text{DELSH} \\
 m_1 &= m_H + m_{UT} + m_{LT} = \text{HNT} \\
 V_1 &= V_H + V_{UT} + V_{LT} \\
 \rho_1 &= m_1/V_1
 \end{aligned} \right\} \quad (\text{A4})$$

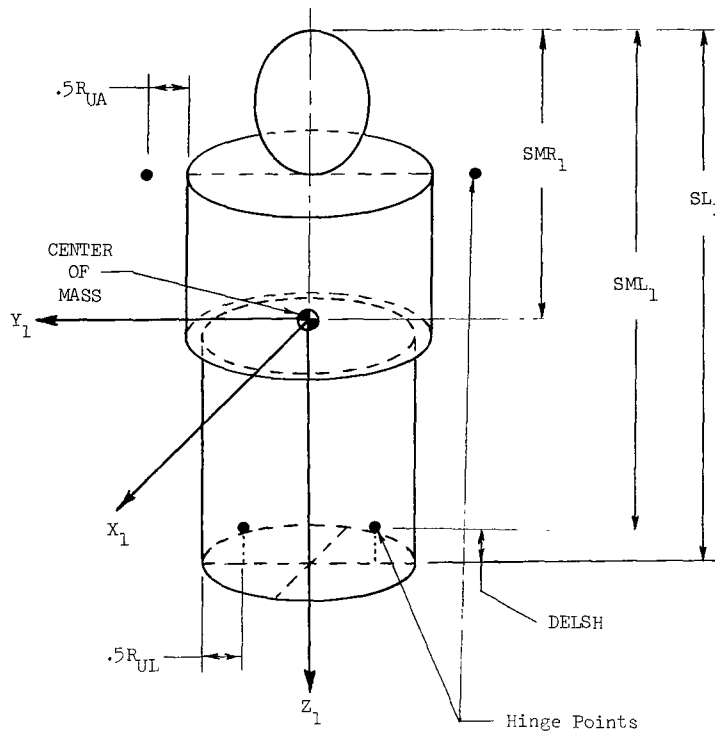


Figure 22.- Segment 1 of model man (from combination of head, upper torso, and lower torso segments).

The distance from the top of the head to the center of mass for this multibody system is

$$\text{SMR}_1 = \frac{m_H \cdot R_H + m_{UT}(\text{SL}_H + \text{SR}_{UT}) + m_{LT}(\text{SL}_H + \text{SL}_{UT} + \text{SR}_{LT})}{\text{HNT}} \quad (\text{A5})$$

The total local moment of inertia about each of the segment reference axes is given by the parallel-axis theorem

APPENDIX A - Continued

$$SI_{XX,1} = SI_{XX,H} + SI_{XX,UT} + SI_{XX,LT} + m_H(SR_H - SMR_1)^2 \\ + m_{UT}(SL_H + SR_{UT} - SMR_1)^2 + m_{LT}(SL_H + SL_{UT} + SR_{LT} - SMR_1)^2 \quad (A6)$$

$$SI_{YY,1} = SI_{YY,H} + SI_{YY,UT} + SI_{YY,LT} + m_H(SR_H - SMR_1)^2 \\ + m_{UT}(SL_H + SR_{UT} - SMR_1)^2 + m_{LT}(SL_H + SL_{UT} + SR_{LT} - SMR_1)^2 \quad (A7)$$

$$SI_{ZZ,1} = ZI_{ZZ,H} + SI_{ZZ,UT} + SI_{ZZ,LT} \quad (A8)$$

Conical segment properties.- In all following development, the properties of conical segments will apply. To simplify the discussion, all necessary conical segment properties are listed.

$$\left. \begin{aligned} V &= SL \cdot \pi(R^2 + RR^2 + R \cdot RR)/3 \\ \mu &= RR/R \\ \sigma &= 1 + \mu + \mu^2 \\ \eta &= (1 + 2\mu + 3\mu^2)/4\sigma \\ AA &= 9(1 + \mu + \mu^2 + \mu^3 + \mu^4)/20\pi\sigma^2 \\ BB &= 3(1 + 4\mu + 10\mu^2 + 4\mu^3 + \mu^4)/80\sigma^2 \\ SR &= \eta \cdot SL \\ SI_{XX} &= AA \cdot m^2/\rho \cdot SL + BB \cdot m \cdot SL^2 \\ SI_{YY} &= SI_{XX} \\ SI_{ZZ} &= 2AA \cdot m^2/\rho \cdot SL \end{aligned} \right\} \quad (A9)$$

Upper arm (segments 2 and 3).- The upper arm segment is represented by the frustum of a right circular cone. This segment is represented in figure 23. The properties and dimensions of the upper arm are given by

APPENDIX A - Continued

$$\left. \begin{aligned}
 R_2 &= AXILC/2\pi \\
 RR_2 &= ELBC/2\pi \\
 SML_2 &= UPARL - R_2 \\
 m_2 &= 0.5BUA \\
 SL_2 &= UPARL \\
 SMR_2 &= SR_2 - R_2
 \end{aligned} \right\} \quad (A10)$$

For this segment, the local moments of inertia and remaining properties are those of a conical segment.

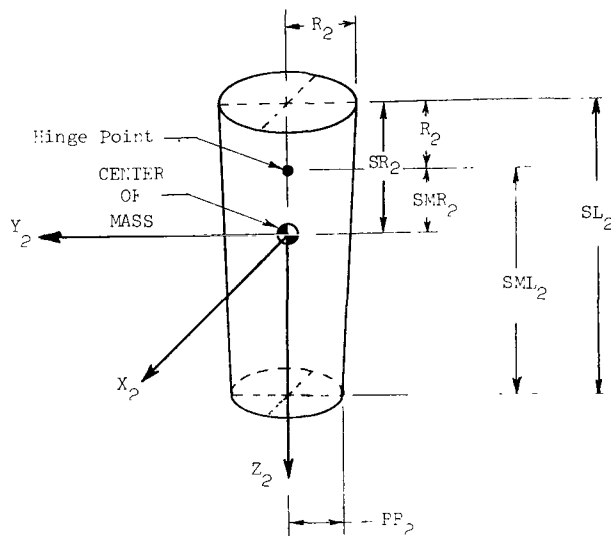


Figure 23.- Upper arm of model man (segments 2 and 3).

Lower arm and hand (segments 4 and 5).- The hand of the model is represented by the sphere shown in figure 24. The properties and dimensions of the hand are given by

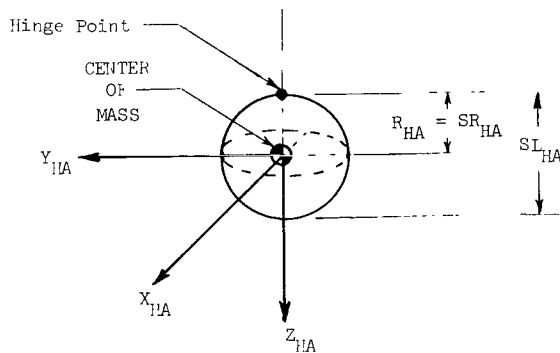
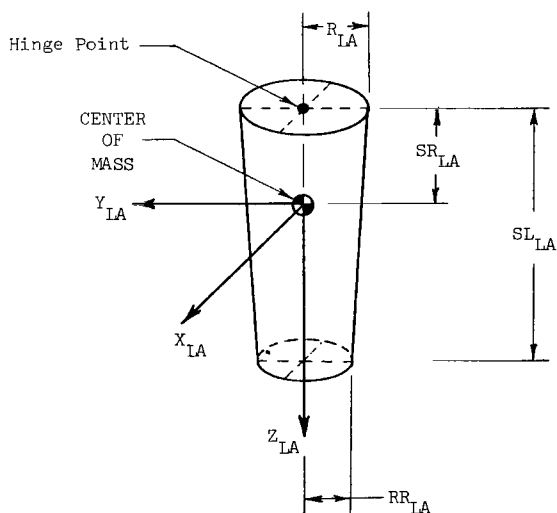


Figure 24.- Hand of model man.

APPENDIX A - Continued

$$\left. \begin{aligned}
 R_{HA} &= FISTC/2\pi \\
 RR_{HA} &= R_{HA} \\
 SL_{HA} &= 2R_{HA} \\
 \eta_{HA} &= 0.5 \\
 m_{HA} &= 0.5BH \\
 SR_{HA} &= R_{HA} \\
 \rho_{HA} &= 3m_{HA}/4\pi \cdot R_{HA}^3 \\
 SI_{XX,HA} &= 0.4m_{HA} \cdot R_{HA}^2 \\
 SI_{YY,HA} &= SI_{XX,HA} \\
 SI_{ZZ,HA} &= SI_{XX,HA}
 \end{aligned} \right\} \quad (A11)$$

The lower arm of the model is represented by a frustum of a right circular cone. The orientation is such as to produce a circular cross section in a plane parallel to the transverse plane. The segment is shown in figure 25. The dimensions and properties of the lower arm are given by



$$\left. \begin{aligned}
 R_{LA} &= ELBC/2\pi \\
 RR_{LA} &= WRISC/2\pi \\
 SL_{LA} &= FOARL \\
 m_{LA} &= 0.5BFO
 \end{aligned} \right\} \quad (A12)$$

Figure 25.- Lower arm of model man.

Local moments of inertia and remaining properties are those of a conical segment.

APPENDIX A – Continued

In figure 26, the assembled lower arm and hand segment is shown. The hand segment and lower arm segment are combined as the total lower arm segment used in the nine-piece model. The dimensions and properties of the combined segment are given by

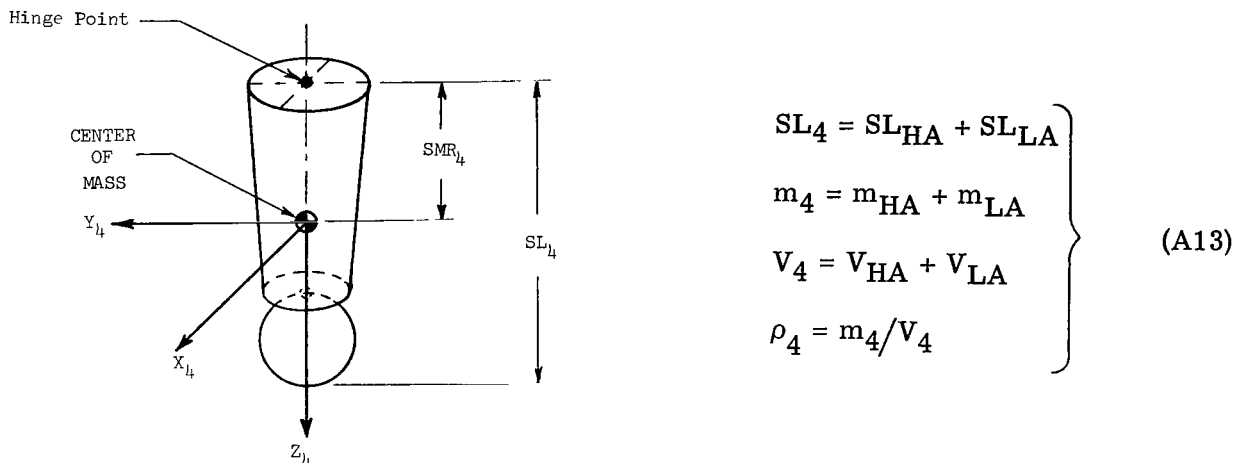


Figure 26.- Segments 4 and 5 of model man (from combination of hand and lower arm segments).

The distance from the hinge point to the center of mass for this multibody system becomes

$$SMR_4 = \frac{m_{HA}(SL_{LA} + SR_{HA}) + m_{LA} \cdot SR_{LA}}{m_4} \quad (A14)$$

The total local moment of inertia about each of the segment reference axes is derived by the parallel-axis theorem, and yields

$$SI_{XX,4} = SI_{XX,HA} + SI_{XX,LA} + m_{HA}(SL_{LA} + SR_{HA} - SMR_4)^2 + m_{LA}(SR_{LA} - SMR_4)^2 \quad (A15)$$

$$SI_{YY,4} = SI_{XX,4} \quad (A16)$$

$$SI_{ZZ,4} = SI_{ZZ,HA} + SI_{ZZ,LA} \quad (A17)$$

Upper leg (segments 6 and 7).- The upper leg of the model is represented by the frustum of a right circular cone. Orientation is such as to produce a circular cross section in a plane parallel to the transverse plane. The segment is illustrated in figure 27. The properties and dimensions of the upper leg are given by

APPENDIX A - Continued

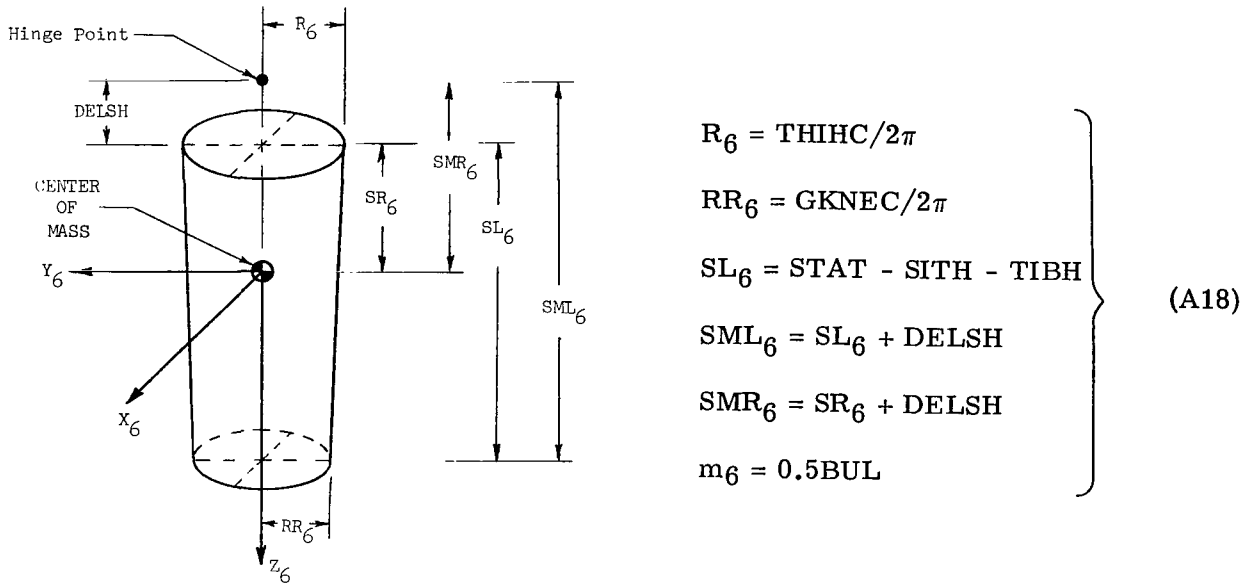


Figure 27.- Upper leg of model man (segments 6 and 7).

Local moments of inertia and remaining properties are those of a conical segment.

Lower leg and foot (segments 8 and 9).- The lower leg of the model is represented by the frustum of a right circular cone. The orientation is such as to produce a circular cross section in a plane parallel to the transverse plane. Figure 28 depicts this subsegment. The properties and dimensions of the lower leg are given by

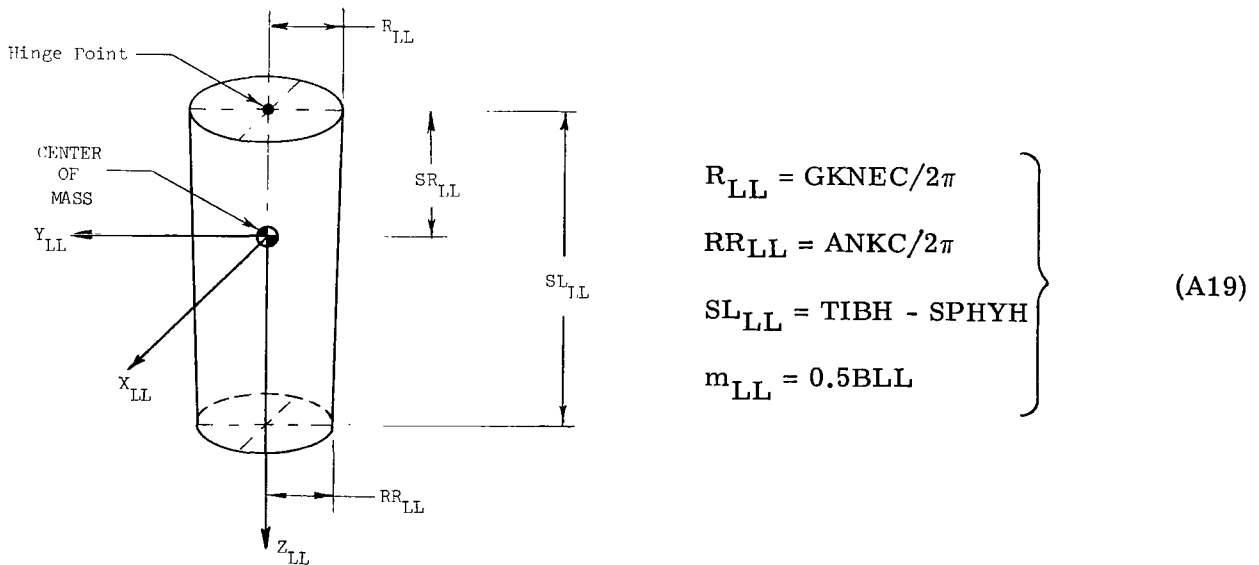


Figure 28.- Lower leg of model man.

APPENDIX A - Continued

The local moments of inertia and remaining properties are those of a conical segment.

The foot of the model is also represented by the frustum of a right circular cone. The orientation is such as to produce a circular cross section in a plane parallel to the frontal plane and a trapezoidal cross section in planes parallel to the transverse and sagittal planes (fig. 29). The dimensions and properties of the foot segment are given by

$$\left. \begin{aligned}
 R_F &= 0.5SPHYH \\
 RR_F &= 0.403R_F \quad (\text{from Dempster, ref. 3}) \\
 SL_F &= FOOTL \\
 m_F &= 0.5BF \\
 \eta_F &= 0.429 \quad (\text{from Dempster, ref. 3})
 \end{aligned} \right\} \quad (A20)$$

The local moments of inertia and the remaining properties are those of a conical segment.

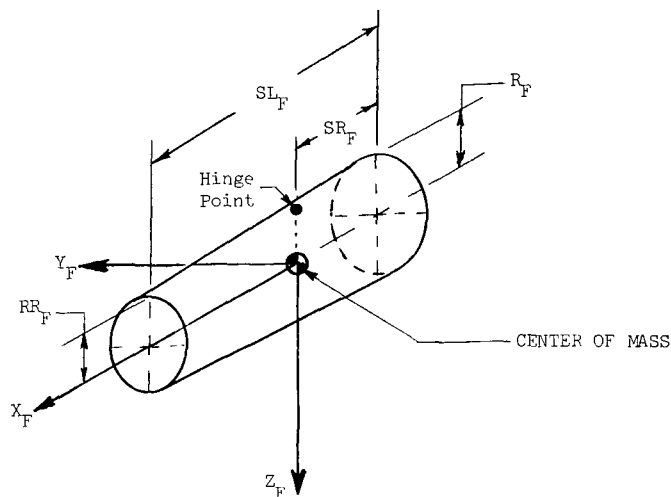


Figure 29.- Foot of model man.

The total lower leg segment of the nine-piece model is composed of the two preceding segments, as shown in figure 30. The dimensions and properties of the combined lower leg segment are given by

$$\left. \begin{aligned}
 SL_8 &= SL_{LL} + SPHYH \\
 V_8 &= V_{LL} + V_F \\
 m_8 &= m_{LL} + m_F \\
 \rho_8 &= m_8/V_8
 \end{aligned} \right\} \quad (A21)$$

APPENDIX A - Continued

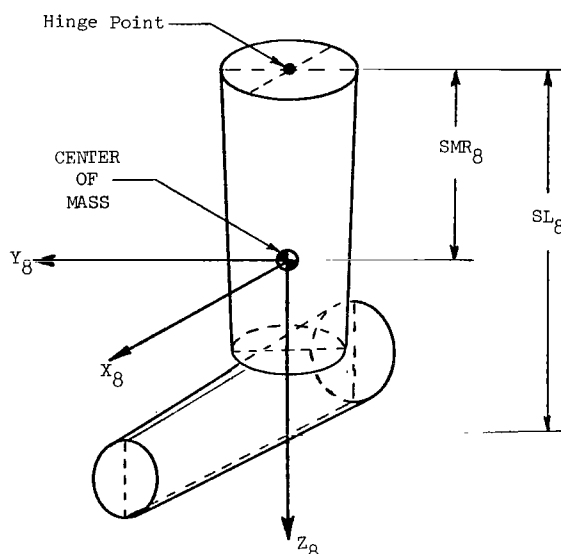


Figure 30.- Segments 8 and 9 of model man (from combination of lower leg and foot segments).

The distance from the hinge point to the center of mass for this multibody system is given by

$$SMR_8 = \frac{m_{LL} \cdot SR_{LL} + m_F(SL_{LL} + R_F)}{m_8} \quad (A22)$$

The total local moments of inertia about each of the segment reference axes follows from the parallel-axis theorem

$$SI_{XX,8} = SI_{XX,LL} + SI_{XX,F} + m_{LL}(SR_{LL} - SMR_8)^2 + m_F(SL_{LL} + R_F - SMR_8)^2 \quad (A23)$$

$$SI_{YY,8} = SI_{YY,LL} + SI_{YY,F} + m_{LL}(SR_{LL} - SMR_8)^2 + m_F(SL_{LL} + R_F - SMR_8)^2 \quad (A24)$$

$$SI_{ZZ,8} = SI_{ZZ,LL} + SI_{ZZ,F} \quad (A25)$$

Comparisons and Extensions

The equations defining segment properties have been incorporated into a computer program, called MAID (for Man's Analytical Inertia Determination), which computes total body inertias and center-of-mass location from the individual segment properties. Inputs required are the subject's mass and the 24 anthropometric measurements listed in table V. Comparison of MAID-computed inertias and center-of-mass location with experimentally measured inertias and center-of-mass locations was performed, using data from Santschi, DuBois, and Omoto (ref. 2). Anthropometric data from 66 Air Force

APPENDIX A – Continued

flight personnel, contained in reference 2, were used as the input to program MAID. The computed data from MAID were then compared with the measured inertial and center-of-mass properties of the same 66 subjects, with the results presented in table VI.

TABLE VI.- COMPARISON OF MEASURED AND COMPUTED  
INERTIAL PROPERTIES FOR ENTIRE MAN

	Santschi et al. (ref. 2) (measured)			MAID (computed)			Average error, percent (ref. 2)
	High	Low	Average	High	Low	Average	
Local moment of inertia about:							
X-axis, kg-m <sup>2</sup>	18.63	8.52	13.00	18.51	8.11	13.05	-0.5
Y-axis, kg-m <sup>2</sup>	16.50	7.49	11.58	17.23	7.61	12.30	-6.2
Z-axis, kg-m <sup>2</sup>	1.97	.77	1.28	1.81	.72	1.10	+13.8
Location of c.m. along Z <sub>MI</sub> -axis, m	0.072	0.059	0.066	0.071	0.060	0.066	0.0

Over the range of the 66 test subjects, there appears to be good agreement between the MAID and experimental results for X- and Y-axis total inertia values and for center-of-mass locations. The larger difference in the Z-axis inertia comparison has been discussed by Hanavan (ref. 5), who performed similar comparisons with his model. Since the moments of inertia for the Z-axis are an order of magnitude smaller than those for the X- and Y-axis, they are subject to larger relative experimental error. It was also pointed out by Hanavan that, upon inspection of documentary photographs taken during the measurements reported in reference 2, it appeared that subjects were not held precisely in position.

The average Z-axis inertia calculated in reference 2 is quite large when compared to that computed by MAID. Since any misalignment with respect to the Z-axis by the subject would cause the measured inertia to be larger than the actual value, the explanation presented by Hanavan appears to be reasonable; the analytical model is not subject to these misalignment errors. The large deviation from experiment for the Z-axis inertial properties should therefore not invalidate the analytical model.

Reference 2 noted that there appears to be a very high degree of correlation between body inertia and total mass. It seemed reasonable to assume that individual segment inertial properties could also be correlated with body mass. Based on the work by Santschi, DuBoise, and Omoto, a linear least-squares analysis was performed to determine

APPENDIX A – Continued

regression equations for local moment of inertia versus total body mass for each segment. The data from the 66 flight personnel, reported in reference 2, were used in the least-squares fit analysis. Results of the least-squares-curve fit are presented as figures 31 to 35. These figures present the experimental data points calculated from the subject dimensions given in reference 2, computed data points for five different percentile cases, and the lines of regression (solid lines), their standard deviations (broken lines), and algebraic equations. Segment moment of inertia is plotted against total body mass for each figure.

The five percentile cases, denoted by inverted triangles on the figures, represent composite, and not actual, subjects. For example, 5th-percentile values were taken from each set of the 24 anthropometric measurements in order to make up the 5th-percentile man. The 5th-, 25th-, 50th-, 75th-, and 95th-percentile cases were computed for each segment inertia and plotted against corresponding subject mass percentile values (60.2 kg, 67.5 kg, 73.6 kg, 80.35 kg, and 91.2 kg, respectively). It can be seen from figures 31 to 35 that the linear-curve fits were very good for all segments as indicated by the small standard deviations. Also, the agreement of the five percentile cases with the regression equations was close. It is thus apparent that the regression equations can be a useful tool in computing segment inertial properties, with only a knowledge of total body mass of a particular subject.

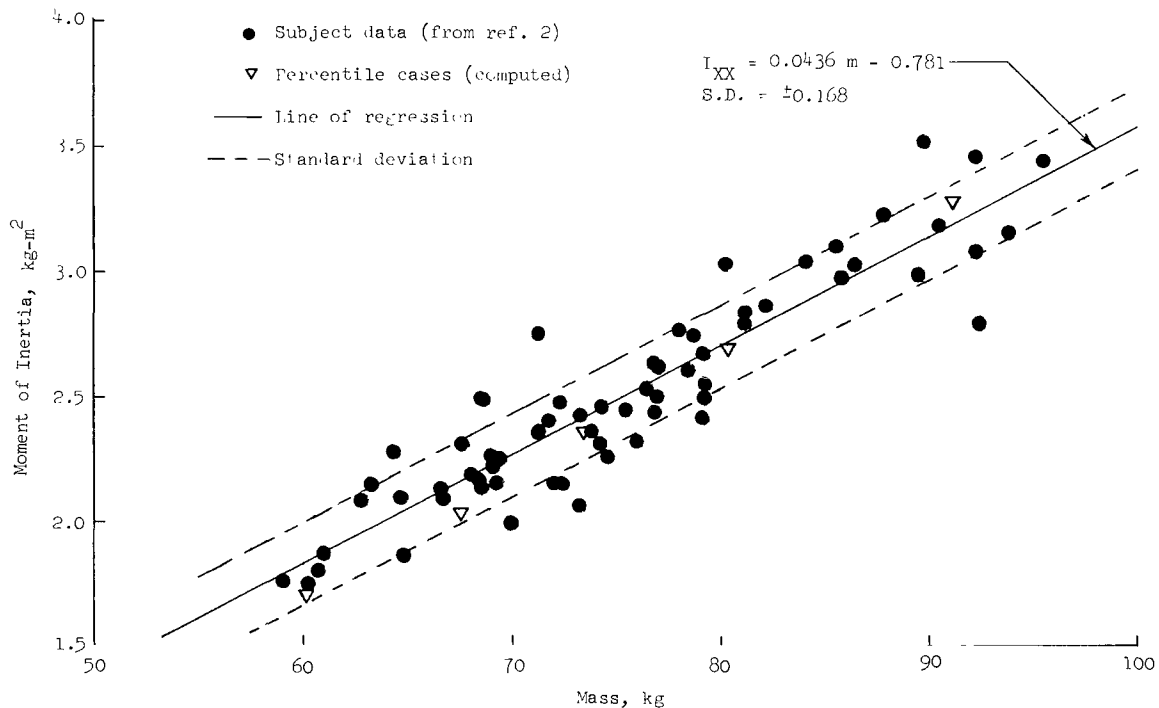


Figure 31.- Variation of segment moment of inertia with man's mass for segment 1 of model man.

APPENDIX A - Continued

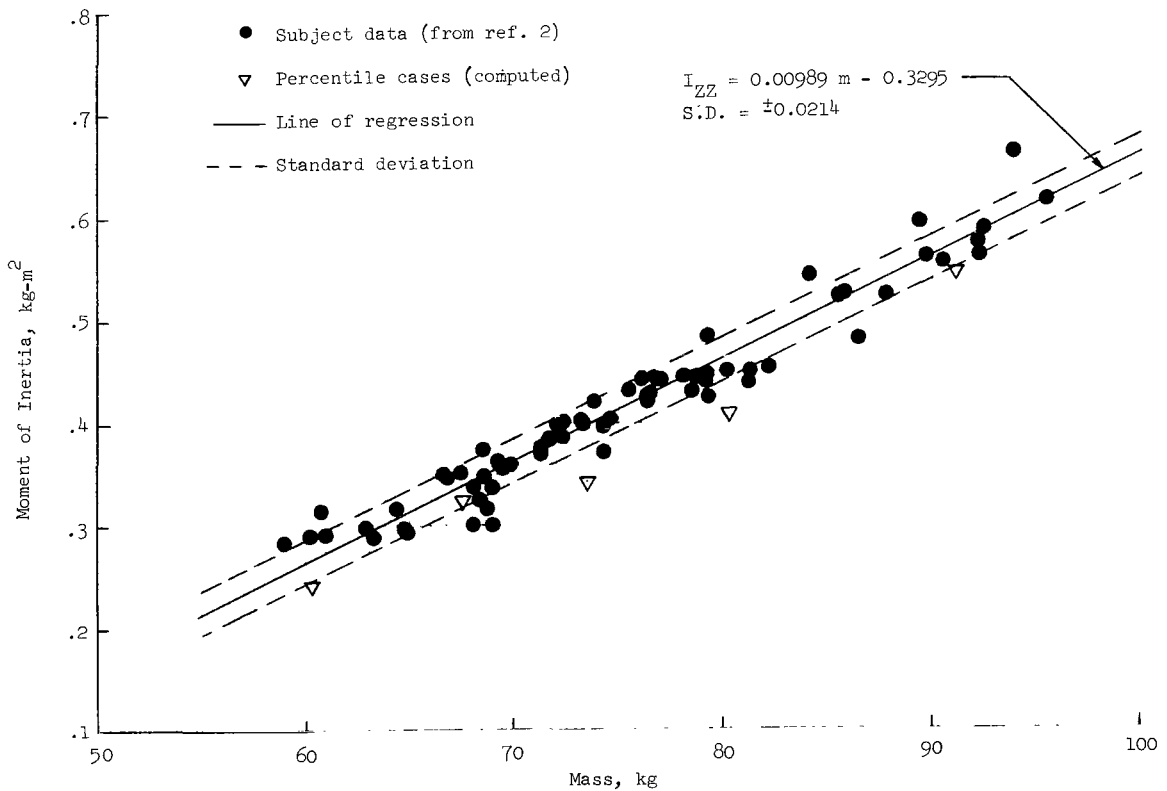
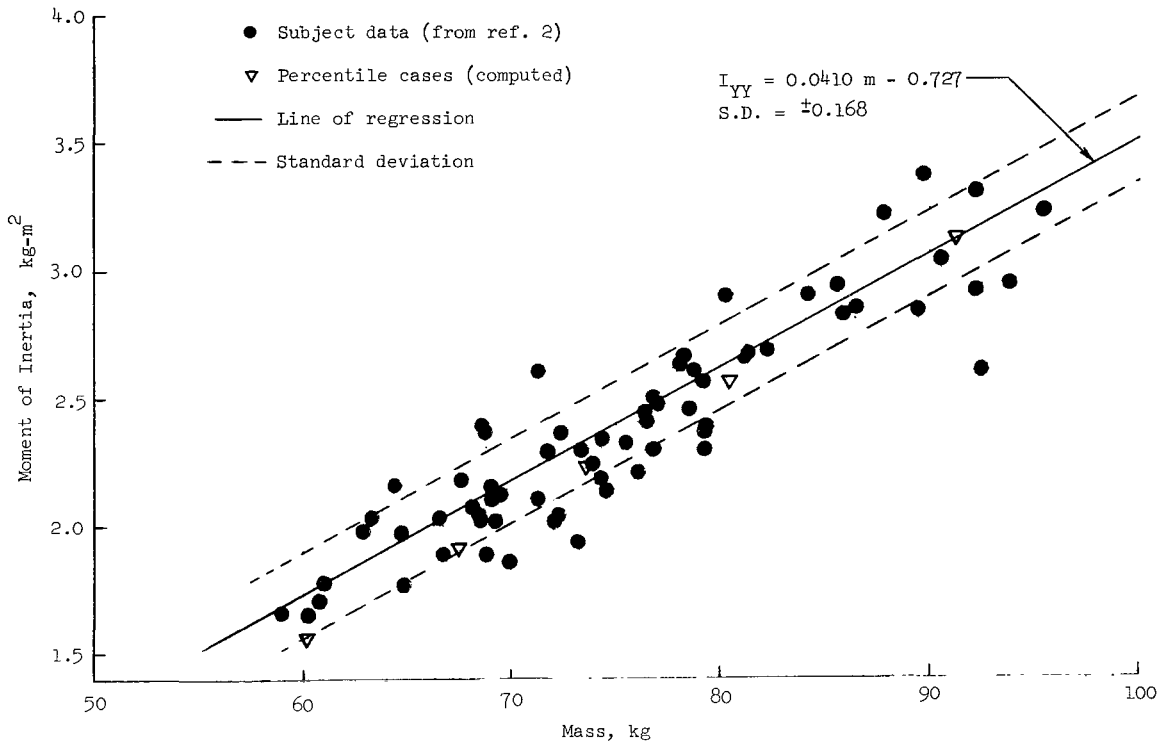


Figure 31.- Concluded.

APPENDIX A - Continued

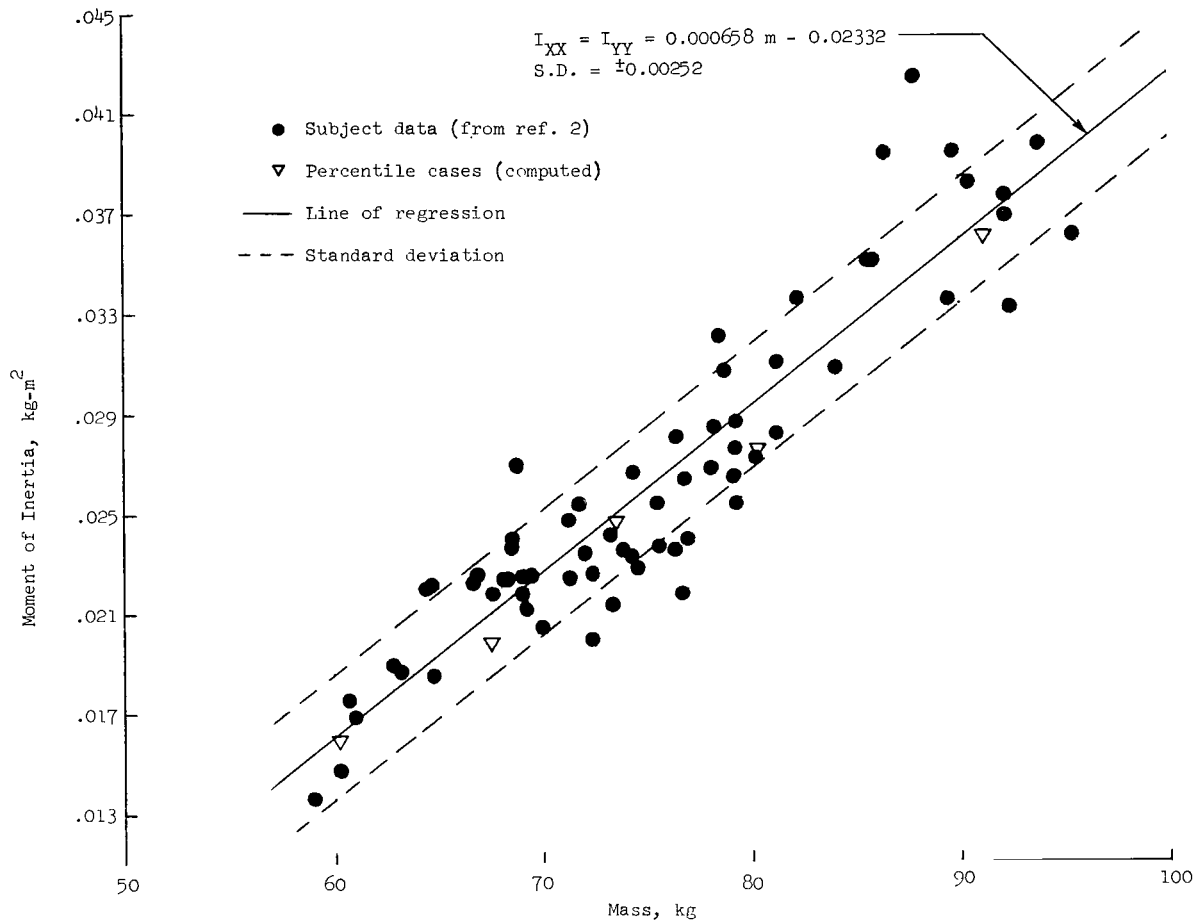


Figure 32.- Variation of segment moment of inertia with man's mass for segments 2 and 3 of model man.

APPENDIX A - Continued

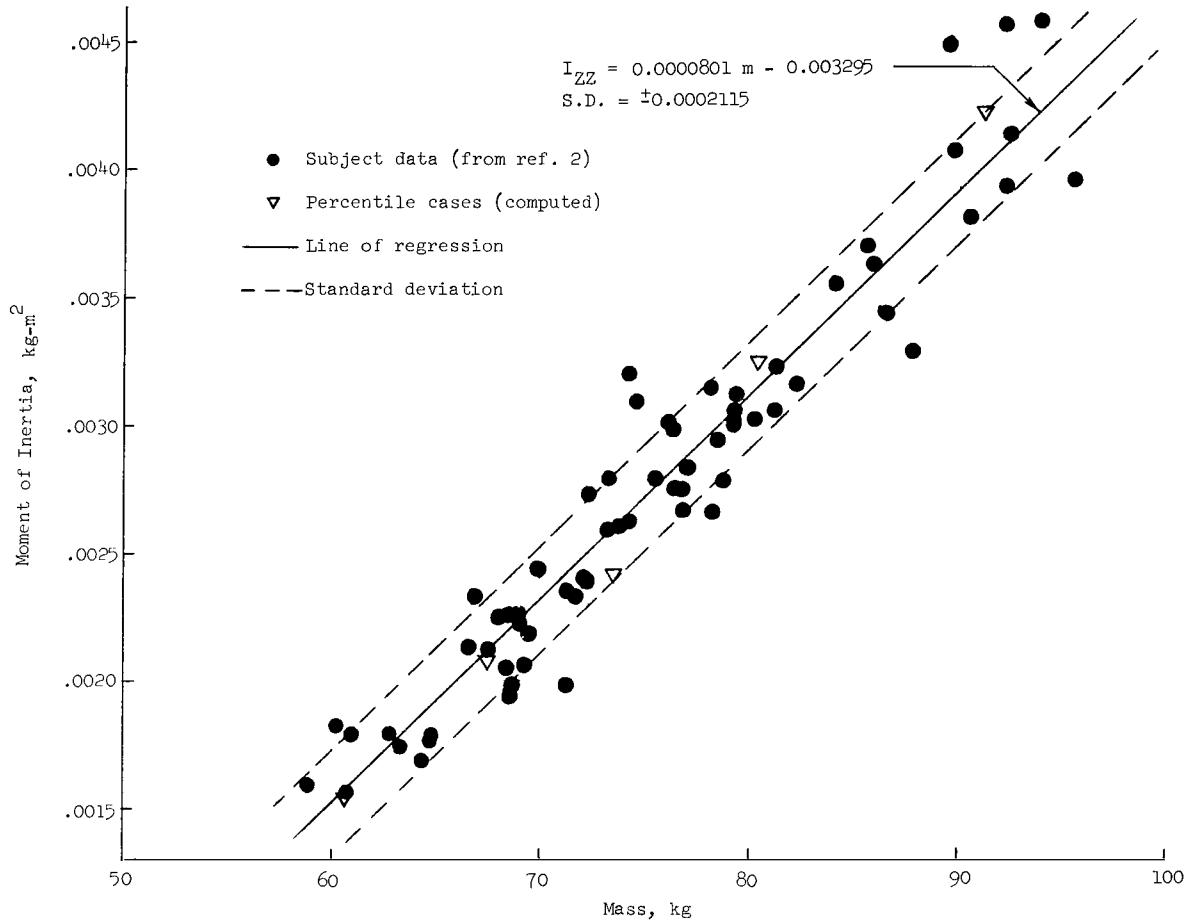


Figure 32.- Concluded.

APPENDIX A - Continued

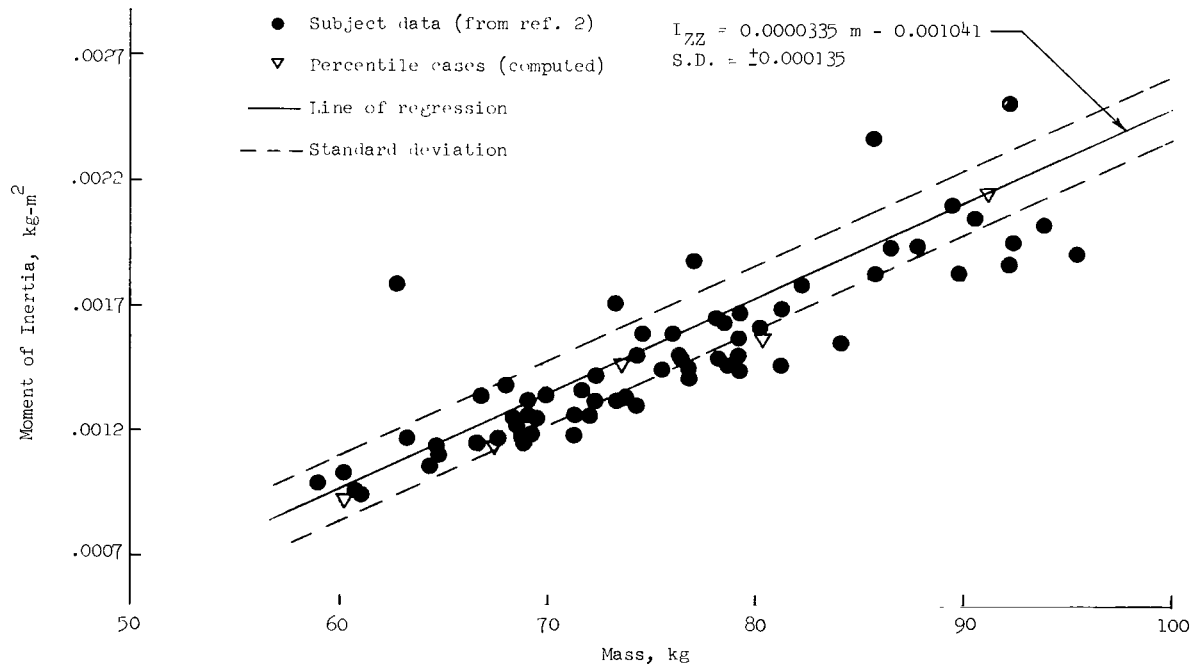
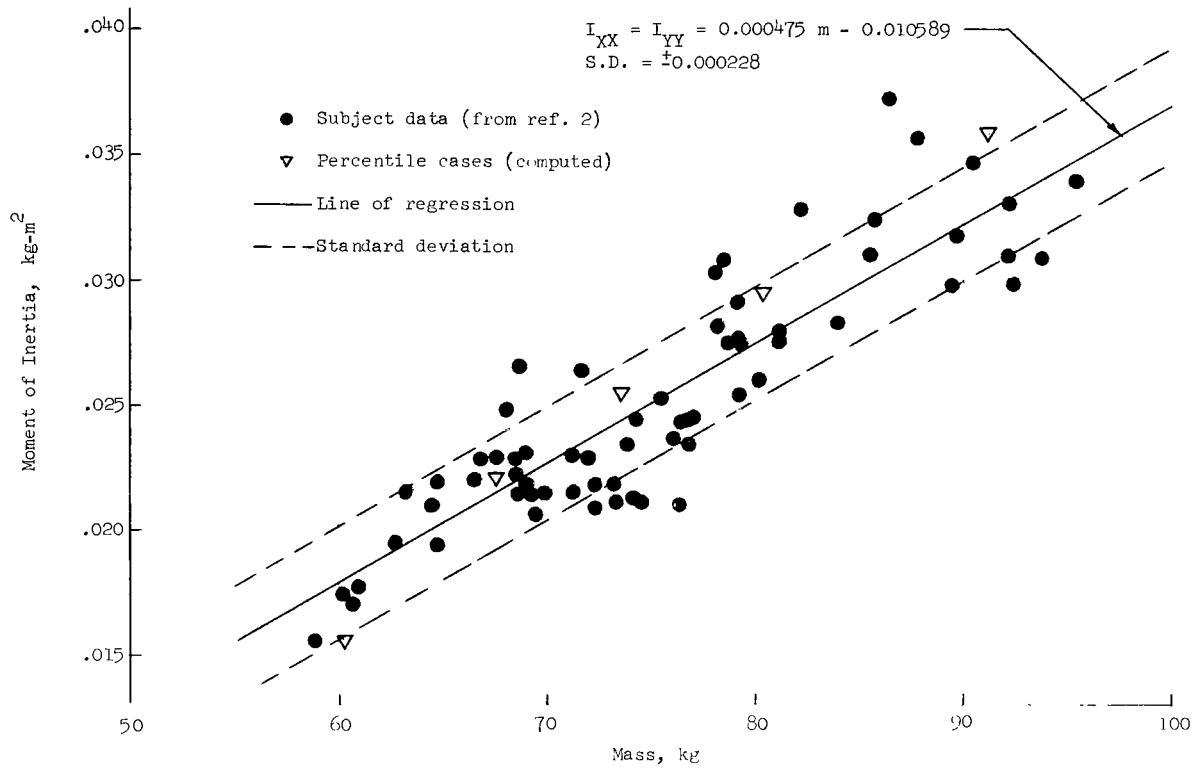


Figure 33.- Variation of segment moment of inertia with man's mass for segments 4 and 5 of model man.

# APPENDIX A - Continued

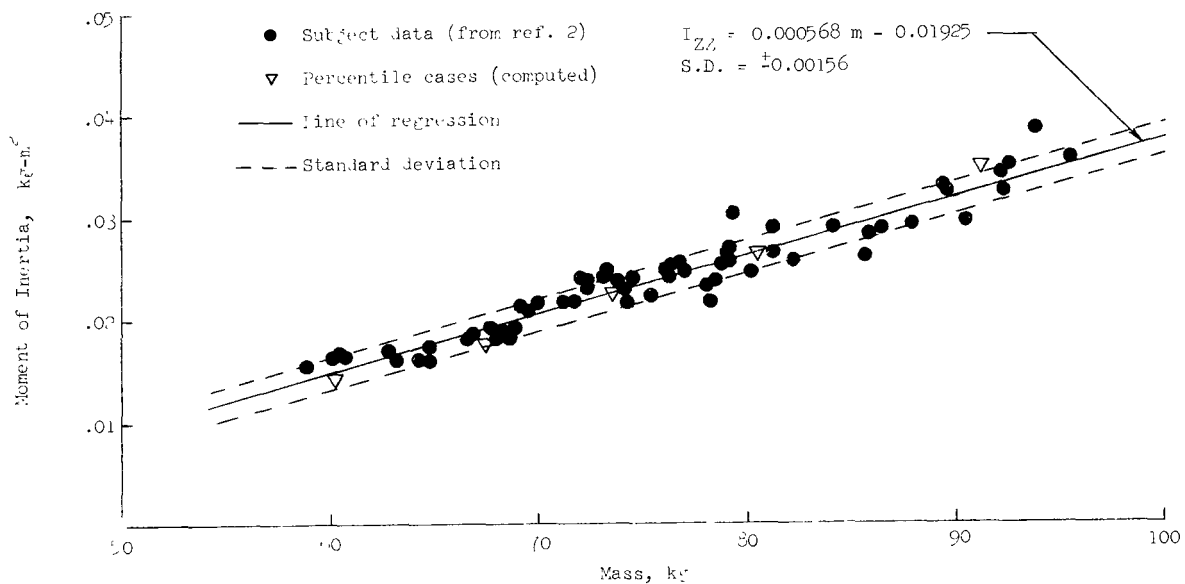
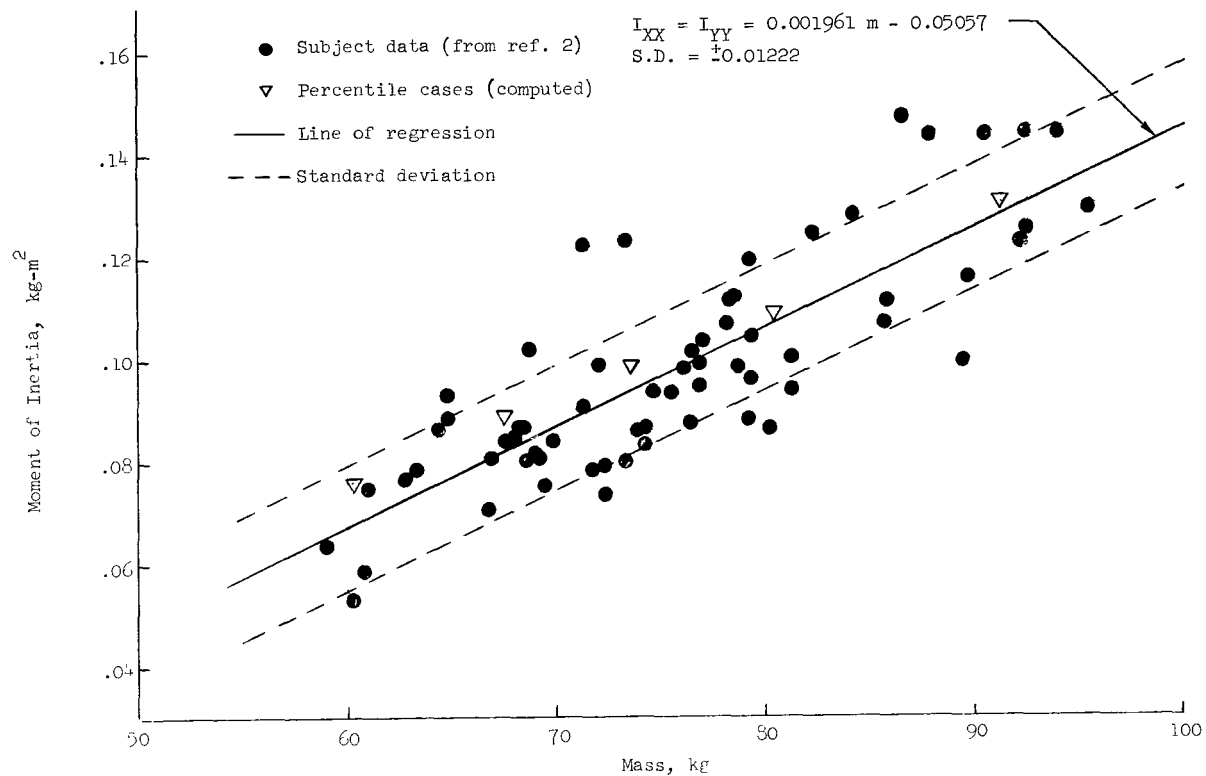


Figure 34.- Variation of segment moment of inertia with man's mass for segments 6 and 7 of model man.

APPENDIX A - Continued

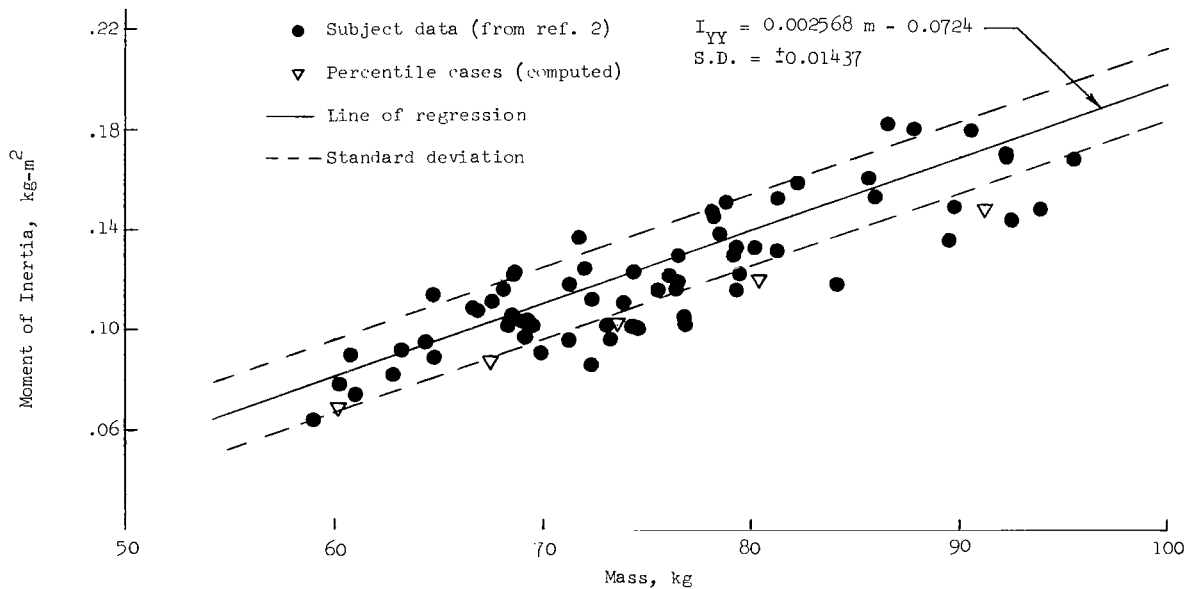
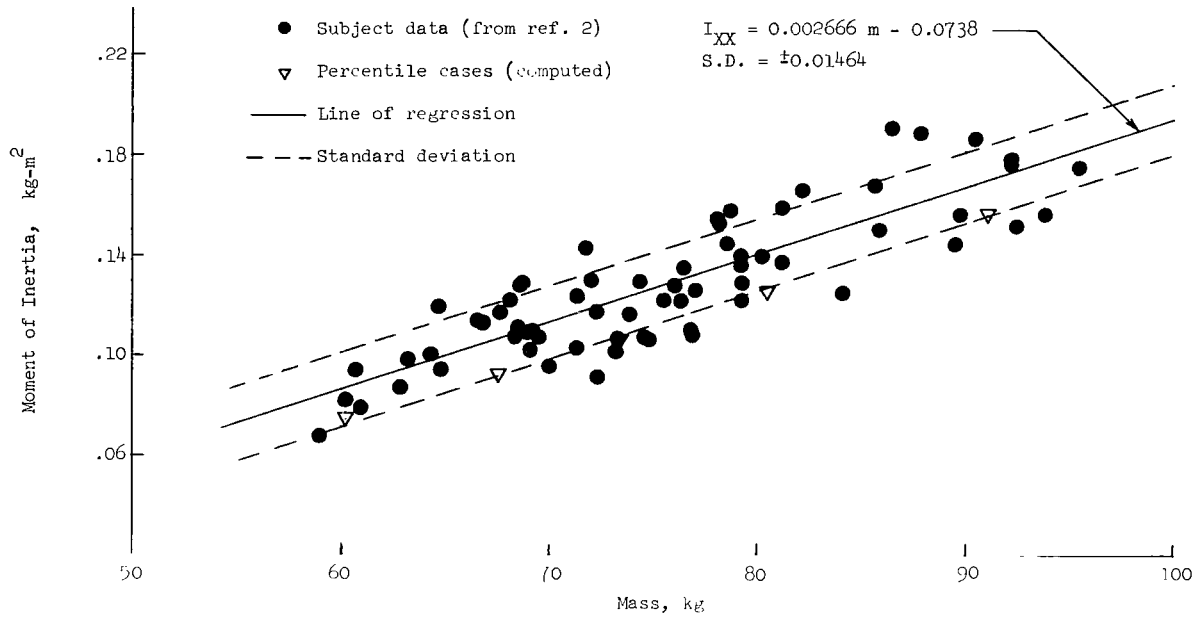


Figure 35.- Variation of segment moment of inertia with man's mass for segments 8 and 9 of model man.

APPENDIX A - Concluded

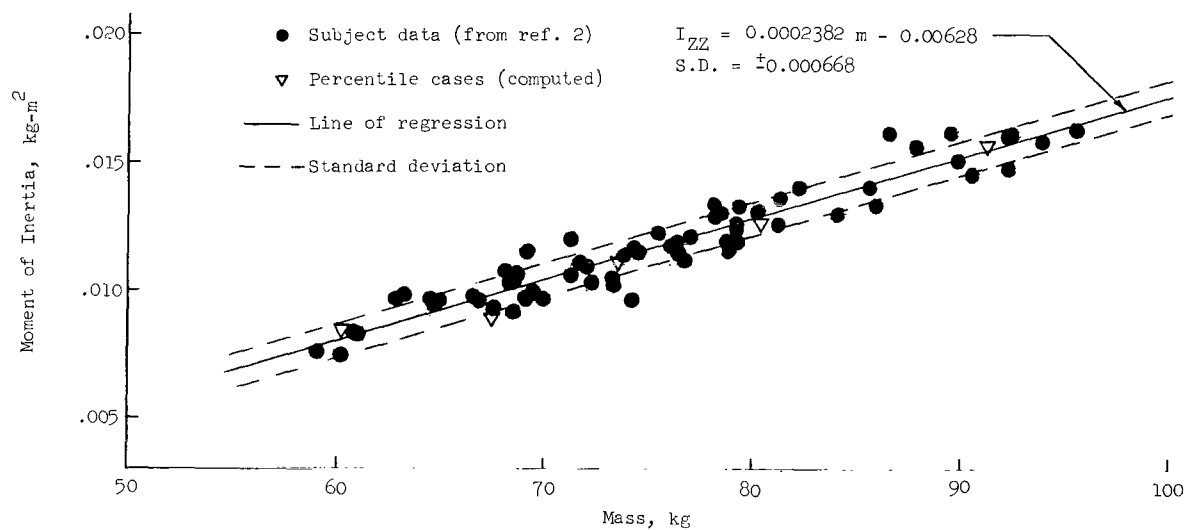


Figure 35.- Concluded.

## APPENDIX B

### DEVELOPMENT OF A DYNAMIC ANALYTICAL MODEL OF MAN ONBOARD A MANNED SPACECRAFT

By Peter R. Kurzhals and Robert B. Reynolds  
Langley Research Center

This appendix utilizes the model man developed in appendix A, and derives applied force and torque equations corresponding to motions of this model. These torque and force equations are incorporated in the rigid-body equations of motion for arbitrary spacecraft. Both the disturbance torque due to crew activity and the effects of these torques on the spacecraft attitude and rates are determined by specifying the motion of the mathematical model within the spacecraft.

#### Reference Coordinates

The reference coordinates for the dynamic-model development are illustrated in figure 36. The spacecraft angular motion is defined by a set of  $X, Y, Z$  of body-fixed axes which rotate with respect to a set  $X_I, Y_I, Z_I$  of intermediate axes. The origin of the  $X, Y, Z$  system is selected as the spacecraft center of mass, without any crew (or model man).

The intermediate axes are free to translate without rotation in inertial space, and always remain parallel to a set  $X_F, Y_F, Z_F$  of inertially fixed axes. The attitude of the spacecraft is described by Euler angles which relate the  $X, Y, Z$ - and  $X_I, Y_I, Z_I$ -axes.

The rotation of the model man is specified by two sets of axes whose origins are coincident with the model center of mass. The  $X_M, Y_M, Z_M$ -set is parallel to the principal axes of segment 1 of the model (torso and head), and rotate relative to the  $X_{MS}, Y_{MS}, Z_{MS}$ -axes, which remain parallel to the  $X, Y, Z$ -axes. The  $+X_M$ -axis points toward the front of the model; the  $+Y_M$ -axis points toward the model's right side; and the  $+Z_M$ -axis points toward the model's feet.

The motion of the model man's center of mass is related to the man's lower pivot points (between torso and upper legs) by rectangular coordinates in a set  $X_{MI}, Y_{MI}, Z_{MI}$  of body-fixed axes. These axes remain parallel to the  $X_M, Y_M, Z_M$ -axes and have their origin at a point halfway between the hinge points noted in figure 18. The total translation of the model's center of mass is given by the sum of the translation of the  $X_{MI}, Y_{MI}, Z_{MI}$ -origin and the translation of the model's mass center with respect to this origin. Mass center coordinates must be expressed as rectangular coordinates in the  $X, Y, Z$ -axis system.

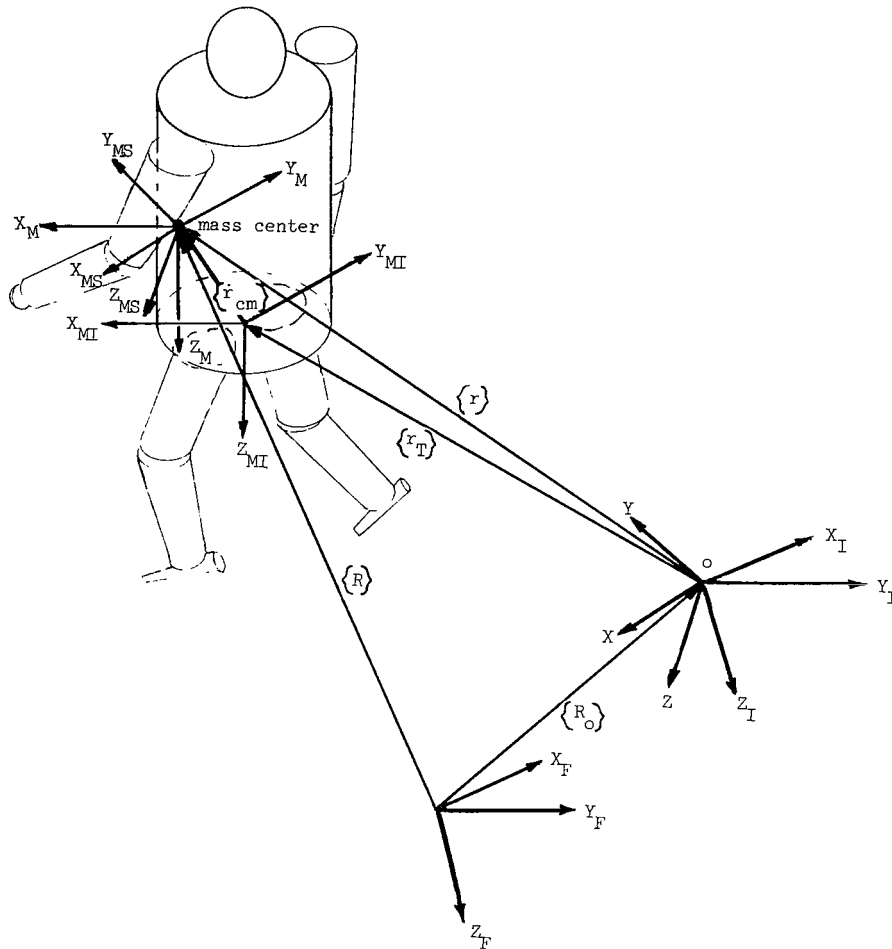


Figure 36.- Reference coordinates used in the development of the dynamic model of man.

The angular position of segment 1 is described by three Euler angles, shown in figure 37, which relate the  $X_M, Y_M, Z_M$ -axes to the  $X_{MS}, Y_{MS}, Z_{MS}$ -axes and hence to the  $X, Y, Z$ -spacecraft-fixed axes. The angular motion of all other body segments is described by two Euler angles per segment, which relate the moving segments to axes parallel to the  $X_M, Y_M, Z_M$ -axes of segment 1, as shown in figure 38.

The model's motion with respect to the spacecraft is defined by specifying the time variation of the origin of the  $X_{MI}, Y_{MI}, Z_{MI}$ -system (or, eventually, the model center of mass) and of the Euler angles for segments 1 to 9.

### Spacecraft Euler Angles

The inertial spacecraft attitude is defined by three modified Euler angles, illustrated in figure 39, which determine the relative motion between the  $X, Y, Z$ - and  $X_I, Y_I, Z_I$ -axes. These modified Euler angles are designated as  $\psi$ ,  $\theta$ , and  $\varphi$ , and result from

APPENDIX B - Continued

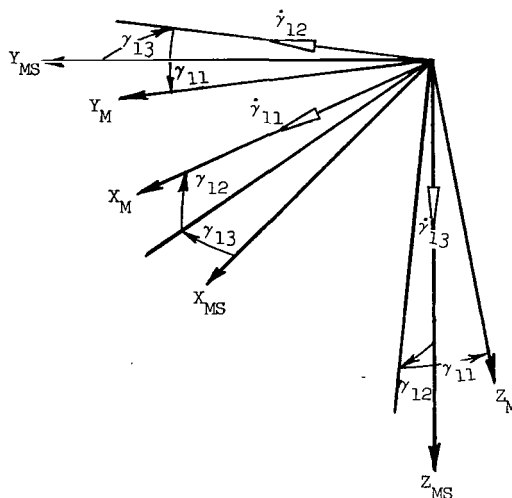


Figure 37.- Euler angles for segment 1 of the dynamic model of man. Rotation sequence is  $\gamma_{13}, \gamma_{12}, \gamma_{11}$ .

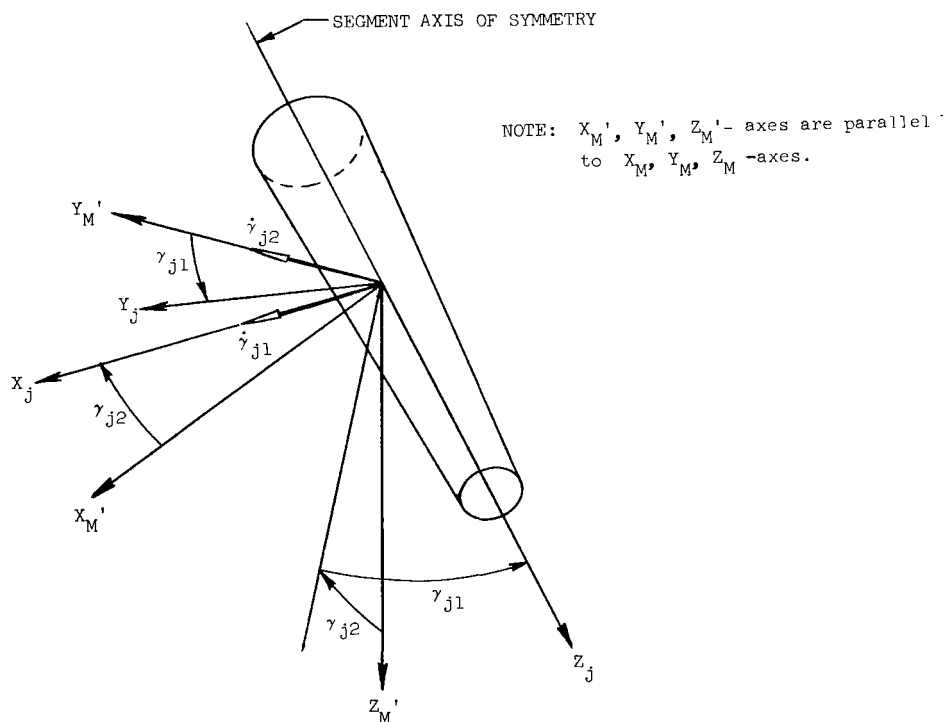


Figure 38.- Euler angles for segments 2 to 9 of the dynamic model of man. Rotation sequence is  $0, \gamma_{j2}, \gamma_{j1}$ .

APPENDIX B – Continued

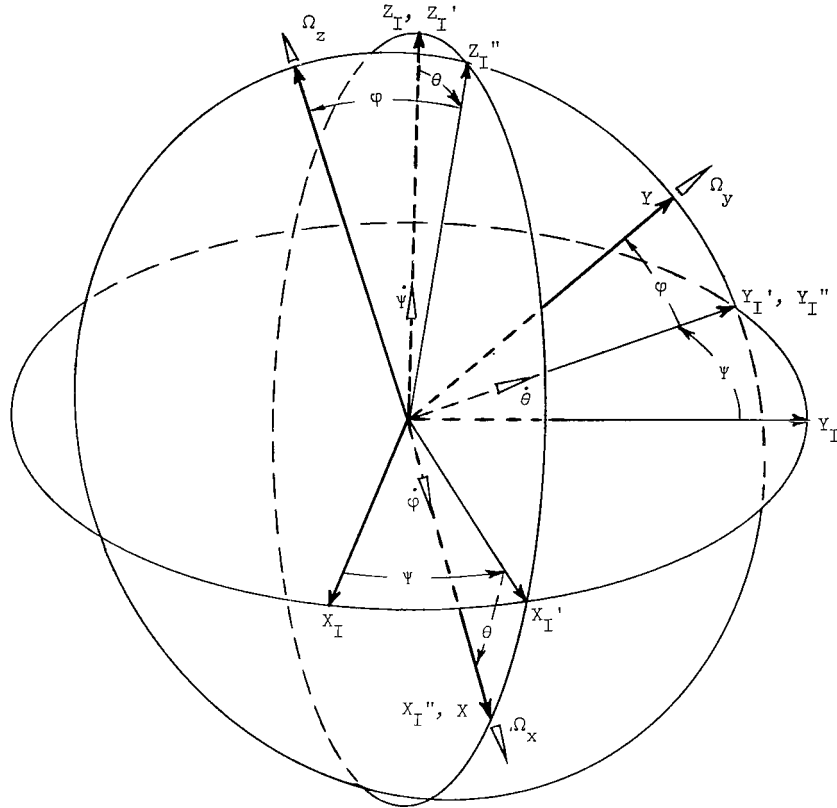


Figure 39.- Euler angles used to describe spacecraft rotations.  
Rotation sequence is  $\psi, \theta, \phi$ .

three consecutive rotations about the  $Z_I, Y_I', X_I''$ -axes. From figure 39, the time derivatives of the Euler angles become

$$\left. \begin{aligned} \dot{\phi} &= \Omega_x + \Omega_y \tan \theta \sin \phi + \Omega_z \tan \theta \cos \phi \\ \dot{\theta} &= \Omega_y \cos \phi - \Omega_z \sin \phi \\ \dot{\psi} &= \Omega_z \cos \phi \sec \theta + \Omega_y \sin \phi \sec \theta \end{aligned} \right\} \quad (B1)$$

The Euler angles can be found by numerical integration of equations (B1), after the body rates  $\Omega_x$ ,  $\Omega_y$ , and  $\Omega_z$  have been derived by the numerical integration of the equations of motion for the spacecraft. Time histories of both the Euler angles and the body rates are used to describe the angular motion of the spacecraft.

Equations of Motion

To develop the equations of motion for the spacecraft and man, the following notation is introduced. Any  $3 \times 1$  vector, such as the spacecraft angular velocity  $\{\Omega\}$  and the man's center of mass position  $\{r\}$ , is designated by braces  $\{\}$ . Any  $3 \times 3$  matrix,

APPENDIX B – Continued

such as the matrix  $[\mathbf{I}_S]$  of the spacecraft inertia tensor, is designated by brackets  $[\ ]$ . A vector symbol which is enclosed by brackets instead of braces represents the skew symmetric matrix corresponding to that vector. For the spacecraft angular velocity

$$\{\Omega\} \equiv \begin{Bmatrix} \Omega_x \\ \Omega_y \\ \Omega_z \end{Bmatrix} \quad (\text{B2})$$

this skew symmetric matrix is

$$[\Omega] \equiv \begin{bmatrix} 0 & -\Omega_z & \Omega_y \\ \Omega_z & 0 & -\Omega_x \\ -\Omega_y & \Omega_x & 0 \end{bmatrix} \quad (\text{B3})$$

A similar matrix can be constructed for any vector.

The moment equation in the geometric spacecraft coordinate axis system  $X, Y, Z$  may now be written as

$$\{\mathbf{M}_E\} + \{\mathbf{M}_M\} = \frac{d\{\mathbf{H}_S\}}{dt} + \frac{m_M}{m_S}[\mathbf{r}]\{\mathbf{F}_S\} \quad (\text{B4})$$

where the external moment  $\{\mathbf{M}_E\}$ , the moment  $\{\mathbf{M}_M\}$  exerted by man, and the radius vector  $\{\mathbf{r}\}$  to the man's center of mass are all referred to the spacecraft geometric origin. The spacecraft angular momentum  $\{\mathbf{H}_S\}$  and the total force  $\{\mathbf{F}_S\}$  are referred to the changing composite mass center of the spacecraft and the moving man.

The moment exerted by crew activity is derived by considering the man as a separate dynamic system whose motion is completely specified in spacecraft coordinates. This leads to a moment expression of the form

$$\{\mathbf{M}_M\} = -\frac{d\{\mathbf{H}_M\}}{dt} - m_M[\mathbf{r}]\frac{d^2\{\mathbf{R}\}}{dt^2} \quad (\text{B5})$$

where  $\{\mathbf{H}_M\}$  is the angular momentum of the man referred to his mass center and  $\{\mathbf{R}\}$  is his mass center radius in fixed (inertial) coordinates. The second term on the right-hand side of equation (B5) represents the torque when the man is taken as a point mass  $m_M$  located by the radius vector  $\{\mathbf{r}\}$  in spacecraft geometric coordinates. The quantity  $-m_M \frac{d^2\{\mathbf{R}\}}{dt^2}$  represents the force that is applied to the spacecraft at the point where the man is in contact with it. Components of this force are measured for the subject of experiment T-013 by the force measuring units.

APPENDIX B - Continued

The acceleration of the man's mass center is given by

$$\begin{aligned} \frac{d^2\{\mathbf{R}\}}{dt^2} &= \{\ddot{\mathbf{R}}_O\} + \frac{d^2\{\mathbf{r}\}}{dt^2} \\ &= \{\ddot{\mathbf{R}}_O\} + \{\ddot{\mathbf{r}}\} + 2[\boldsymbol{\Omega}]\{\dot{\mathbf{r}}\} + [\dot{\boldsymbol{\Omega}}]\{\mathbf{r}\} + [\boldsymbol{\Omega}][\boldsymbol{\Omega}]\{\mathbf{r}\} \end{aligned} \quad (\text{B6})$$

where  $\{\mathbf{R}_O\}$  is the position vector in fixed coordinates to the spacecraft geometric origin. Since

$$\{\mathbf{F}_S\} = \{\mathbf{F}_E\} - m_S \left( \{\ddot{\mathbf{R}}_O\} + \frac{m_M}{m_S} \frac{d^2\{\mathbf{r}\}}{dt^2} \right) \quad (\text{B7})$$

where  $\{\mathbf{F}_E\}$  denotes any external force, the torque produced by the total spacecraft force  $\{\mathbf{F}_S\}$  and the torque produced by man taken as a point mass can now be combined as

$$\begin{aligned} m_M[\mathbf{r}] \left( \{\ddot{\mathbf{R}}_O\} + \frac{d^2\{\mathbf{r}\}}{dt^2} - \{\ddot{\mathbf{R}}_O\} - \frac{m_M}{m_S} \frac{d^2\{\mathbf{r}\}}{dt^2} + \frac{1}{m_S} \{\mathbf{F}_E\} \right) \\ = \frac{m_M(m_S - m_M)}{m_S} [\mathbf{r}] \frac{d^2\{\mathbf{r}\}}{dt^2} + \frac{m_M}{m_S} [\mathbf{r}] \{\mathbf{F}_E\} \end{aligned} \quad (\text{B8})$$

Substitution of equations (B5) and (B8) into equation (B4) yields

$$\{\mathbf{M}_E\} - \frac{d\{\mathbf{H}_M\}}{dt} = \frac{d\{\mathbf{H}_S\}}{dt} + \frac{m_M(m_S - m_M)}{m_S} [\mathbf{r}] \frac{d^2\{\mathbf{r}\}}{dt^2} + \frac{m_M}{m_S} [\mathbf{r}] \{\mathbf{F}_E\} \quad (\text{B9})$$

Let

$$\mathbf{T} = - \frac{d\{\mathbf{H}_M\}}{dt} \quad (\text{B10})$$

and

$$\mathbf{Q} = \frac{m_M(m_S - m_M)}{m_S} \quad (\text{B11})$$

to get

$$\{\mathbf{M}_E\} + \{\mathbf{T}\} = \frac{d\{\mathbf{H}_S\}}{dt} + \mathbf{Q}[\mathbf{r}] \frac{d^2\{\mathbf{r}\}}{dt^2} + \frac{m_M}{m_S} [\mathbf{r}] \{\mathbf{F}_E\} \quad (\text{B12})$$

$$\{\mathbf{H}_S\} = [\mathbf{I}_S] \{\boldsymbol{\Omega}\} \quad (\text{B13})$$

APPENDIX B - Continued

and

$$[I_S] = \begin{bmatrix} I_{XS} & -I_{XYS} & -I_{XZS} \\ -I_{XYS} & I_{YS} & -I_{YZS} \\ -I_{XZS} & -I_{YZS} & I_{ZS} \end{bmatrix} \quad (B14)$$

In the expanded form the equations of motion represented by equation (B12) become

$$\begin{aligned} \{M_E\} + \{T\} = [I_S] \{\dot{\Omega}\} + [\Omega][I_S] \{\Omega\} + Q[r] \left( \{\ddot{r}\} + 2[\Omega] \{\dot{r}\} \right. \\ \left. + [\dot{\Omega}] \{r\} + [\Omega][\Omega] \{r\} \right) + \frac{m_M}{m_S} [r] \{F_E\} \end{aligned} \quad (B15)$$

For this development, it is convenient to introduce a total angular momentum given by

$$\{H_T\} = \{H_S\} + Q[r] \frac{d\{r\}}{dt} \quad (B16)$$

which is equal to the angular momentum of the spacecraft and the moving man taken as a point mass. Equation (B16) can be rewritten in terms of the familiar "rigid-body" angular momentum, denoted by  $\{H_{RB}\}$ , which is formulated in terms of the instantaneous inertia of the spacecraft and point-mass man and the spacecraft angular rates. The result is

$$\{H_T\} = \{H_{RB}\} + Q[r] \{\dot{r}\} \quad (B17)$$

where

$$\{H_{RB}\} = [I_S] \{\Omega\} + Q[r] [\Omega] \{r\} = [I] \{\Omega\} \quad (B18)$$

with

$$[I] = \begin{bmatrix} I_X & -I_{XY} & -I_{XZ} \\ -I_{XY} & I_Y & -I_{YZ} \\ -I_{XZ} & -I_{YZ} & I_Z \end{bmatrix} \quad (B19)$$

Substitution of equations (B16), (B17), and (B18) into equation (B12) yields

$$\begin{aligned} \{M_E\} + \{T\} = \frac{d\{H_T\}}{dt} + \frac{m_M}{m_S} [r] \{F_E\} \\ = \frac{d\{H_{RB}\}}{dt} + Q \left( [r] \{\ddot{r}\} + [\Omega][r] \{\dot{r}\} \right) + \frac{m_M}{m_S} [r] \{F_E\} \end{aligned} \quad (B20)$$

or

$$\begin{aligned} \{M_E\} + \{T\} = & [I]\{\dot{\Omega}\} + [\dot{I}]\{\Omega\} + [\Omega][I]\{\Omega\} \\ & + Q\left([r]\{\ddot{r}\} + [\Omega][r]\{\dot{r}\}\right) + \frac{m_M}{m_S}[r]\{F_E\} \end{aligned} \quad (B21)$$

as the final equations of motion.

### Spacecraft Inertia and Mass Center Coordinate Terms

The spacecraft inertia terms in equations (B19) and (B21) may be written in terms of the spacecraft inertias (excluding the model man), the mass factor  $Q$ , and the Cartesian components of the man's center of mass radius vector  $\{r\}$  as

$$\left. \begin{aligned} I_X &= I_{XS} + Q(y^2 + z^2) \\ I_Y &= I_{YS} + Q(x^2 + z^2) \\ I_Z &= I_{ZS} + Q(x^2 + y^2) \\ I_{XY} &= I_{XYS} + Q(xy) \\ I_{XZ} &= I_{YZS} + Q(xz) \\ I_{YZ} &= I_{YZS} + Q(yz) \end{aligned} \right\} \quad (B22)$$

The time derivatives of the inertia terms, which appear in equation (B21), become

$$\left. \begin{aligned} \dot{I}_X &= 2Q(y\dot{y} + z\dot{z}) \\ \dot{I}_Y &= 2Q(x\dot{x} + z\dot{z}) \\ \dot{I}_Z &= 2Q(x\dot{x} + y\dot{y}) \\ \dot{I}_{XY} &= Q(x\dot{y} + y\dot{x}) \\ \dot{I}_{XZ} &= Q(x\dot{z} + z\dot{x}) \\ \dot{I}_{YZ} &= Q(y\dot{z} + z\dot{y}) \end{aligned} \right\} \quad (B23)$$

The radius vector  $\{r\}$  to the center of mass of the mathematical model of man is specified by

$$\{r\} = \{r_T\} + \{r_{cm}\} \quad (B24)$$

where  $\{r_T\}$  is the radius from the spacecraft geometric origin to the origin of the  $X_{MI}, Y_{MI}, Z_{MI}$ -axis system, and  $\{r_{cm}\}$  is the radius vector from the  $X_{MI}, Y_{MI}, Z_{MI}$ -origin to the mass center of the model man. Remembering that  $\{r\}$  must be expressed in X,Y,Z-coordinates,  $\{r_{cm}\}$  is expressed in that system by the transformation

$$\{r_{cm}\} = \begin{Bmatrix} x_{cm} \\ y_{cm} \\ z_{cm} \end{Bmatrix} = [D_1] \begin{Bmatrix} x_{MI} \\ y_{MI} \\ z_{MI} \end{Bmatrix} = [D_1] \{r_{MI}\} \quad (B25)$$

The Euler angle transformation matrix  $[D_1]$  for segment 1 of the mass center coordinates  $x_{MI}$ ,  $y_{MI}$ , and  $z_{MI}$  in the  $X_{MI}, Y_{MI}, Z_{MI}$ -system are defined in subsequent sections of this appendix.

Time derivatives of  $\{r\}$  are needed in the equations of motion and are given by

$$\{\dot{r}\} = \{\dot{r}_T\} + [\dot{D}_1] \{r_{MI}\} + [D_1] \{\dot{r}_{MI}\} \quad (B26)$$

and

$$\{\ddot{r}\} = \{\ddot{r}_T\} + [\ddot{D}_1] \{r_{MI}\} + 2[\dot{D}_1] \{\dot{r}_{MI}\} + [D_1] \{\ddot{r}_{MI}\} \quad (B27)$$

### Segment Transformation Matrices

Quantities measured relative to the  $X_M, Y_M, Z_M$ - or  $X_{MI}, Y_{MI}, Z_{MI}$ -axes may be referred to the  $X, Y, Z$ -system by means of the transformation matrix  $[D_1]$ ; likewise, quantities measured relative to the segment coordinate axes  $X_j, Y_j, Z_j$  ( $j = 2, 3, 4, \dots, 9$ ) may be referred to the  $X_M, Y_M, Z_M$ -axes by means of the transformation matrices  $[D_j]$ , where  $j = 2, 3, \dots, 9$ .

Matrices required for the transformation process are ( $j = 1, 2, \dots, 9$  in each case)

$$[D_j] \equiv \begin{bmatrix} jd_{11} & jd_{12} & jd_{13} \\ jd_{21} & jd_{22} & jd_{23} \\ jd_{31} & jd_{32} & jd_{33} \end{bmatrix} \quad (B28a)$$

$$[\dot{D}_j] \equiv \begin{bmatrix} j\dot{d}_{11} & j\dot{d}_{12} & j\dot{d}_{13} \\ j\dot{d}_{21} & j\dot{d}_{22} & j\dot{d}_{23} \\ j\dot{d}_{31} & j\dot{d}_{32} & j\dot{d}_{33} \end{bmatrix} \quad (B28b)$$

$$[\ddot{D}_j] \equiv \begin{bmatrix} j\ddot{d}_{11} & j\ddot{d}_{12} & j\ddot{d}_{13} \\ j\ddot{d}_{21} & j\ddot{d}_{22} & j\ddot{d}_{23} \\ j\ddot{d}_{31} & j\ddot{d}_{32} & j\ddot{d}_{33} \end{bmatrix} \quad (B28c)$$

$$\left[ D_j^{-1} \right] = \begin{bmatrix} jd_{11}^{-1} & jd_{12}^{-1} & jd_{13}^{-1} \\ jd_{21}^{-1} & jd_{22}^{-1} & jd_{23}^{-1} \\ jd_{31}^{-1} & jd_{32}^{-1} & jd_{33}^{-1} \end{bmatrix} \quad (B28d)$$

For segment 1

$$\left[ D_1 \right] = \begin{bmatrix} \cos \gamma_{13} \cos \gamma_{12} & \cos \gamma_{13} \sin \gamma_{12} \sin \gamma_{11} & \cos \gamma_{13} \sin \gamma_{12} \cos \gamma_{11} \\ & - \sin \gamma_{13} \cos \gamma_{11} & + \sin \gamma_{13} \sin \gamma_{11} \\ \sin \gamma_{13} \cos \gamma_{12} & \sin \gamma_{13} \sin \gamma_{12} \sin \gamma_{11} & \sin \gamma_{13} \sin \gamma_{12} \cos \gamma_{11} \\ & + \cos \gamma_{13} \cos \gamma_{11} & - \cos \gamma_{13} \sin \gamma_{11} \\ -\sin \gamma_{12} & \cos \gamma_{12} \sin \gamma_{11} & \cos \gamma_{12} \cos \gamma_{11} \end{bmatrix} \quad (B29)$$

For segments 2 to 9

$$\left[ D_j \right] = \begin{bmatrix} \cos \gamma_{j2} & \sin \gamma_{j2} \sin \gamma_{j1} & \sin \gamma_{j2} \cos \gamma_{j1} \\ 0 & \cos \gamma_{j1} & -\sin \gamma_{j1} \\ -\sin \gamma_{j2} & \cos \gamma_{j2} \sin \gamma_{j1} & \cos \gamma_{j2} \cos \gamma_{j1} \end{bmatrix} \quad (j = 2, 3, \dots, 9) \quad (B30)$$

For all segments

$$\left[ \dot{D}_j \right] = \begin{bmatrix} \frac{d(jd_{11})}{dt} & \frac{d(jd_{12})}{dt} & \frac{d(jd_{13})}{dt} \\ \frac{d(jd_{21})}{dt} & \frac{d(jd_{22})}{dt} & \frac{d(jd_{23})}{dt} \\ \frac{d(jd_{31})}{dt} & \frac{d(jd_{32})}{dt} & \frac{d(jd_{33})}{dt} \end{bmatrix} \quad (j = 1, 2, \dots, 9) \quad (B31)$$

$$\left[ \ddot{D}_j \right] = \begin{bmatrix} \frac{d^2(jd_{11})}{dt^2} & \frac{d^2(jd_{12})}{dt^2} & \frac{d^2(jd_{13})}{dt^2} \\ \frac{d^2(jd_{21})}{dt^2} & \frac{d^2(jd_{22})}{dt^2} & \frac{d^2(jd_{23})}{dt^2} \\ \frac{d^2(jd_{31})}{dt^2} & \frac{d^2(jd_{32})}{dt^2} & \frac{d^2(jd_{33})}{dt^2} \end{bmatrix} \quad (j = 1, 2, \dots, 9) \quad (B32)$$

$$[\bar{D}_j]^{-1} = [D_j]^T \quad (j = 1, 2, \dots, 9) \quad (B33)$$

It should be noted that  $[\ddot{D}_j]$  is needed only for  $j = 1$  (i.e., for segment 1).

### Model and Segment Mass Centers in Model Coordinates

By assigning center of mass and pivot-point coordinates to the mathematical model of figure 17, one arrives at the system shown in figure 18.

The segment center-of-mass coordinates, in the  $X_{MI}, Y_{MI}, Z_{MI}$ -system can be readily derived from figures 18 to 30 with the result

$$\begin{Bmatrix} x_{1MI} \\ y_{1MI} \\ z_{1MI} \end{Bmatrix} = \begin{Bmatrix} 0 \\ 0 \\ -SML_1 + SMR_1 \end{Bmatrix} \quad (B34)$$

$$\begin{Bmatrix} x_{2MI} \\ y_{2MI} \\ z_{2MI} \end{Bmatrix} = \begin{Bmatrix} SMR_2 \sin \gamma_{22} \cos \gamma_{21} \\ R_{UT} + R_2 - SMR_2 \sin \gamma_{21} \\ -SML_1 + S_{LH} + SMR_2 \cos \gamma_{22} \cos \gamma_{21} \end{Bmatrix} \quad (B35)$$

$$\begin{Bmatrix} x_{3MI} \\ y_{3MI} \\ z_{3MI} \end{Bmatrix} = \begin{Bmatrix} SMR_2 \sin \gamma_{32} \cos \gamma_{31} \\ -R_{UT} - R_2 - SMR_2 \sin \gamma_{31} \\ -SML_1 + S_{LH} + SMR_2 \cos \gamma_{32} \cos \gamma_{31} \end{Bmatrix} \quad (B36)$$

$$\begin{Bmatrix} x_{4MI} \\ y_{4MI} \\ z_{4MI} \end{Bmatrix} = \begin{Bmatrix} \frac{SML_2}{SMR_2} x_{2MI} + SMR_4 \sin \gamma_{42} \cos \gamma_{41} \\ R_{UT} + R_2 + \frac{SML_2}{SMR_2} (y_{2MI} - R_{UT} - R_2) - SMR_4 \sin \gamma_{41} \\ (-SML_1 + S_{LH}) \left( 1 - \frac{SML_2}{SMR_2} \right) + \frac{SML_2}{SMR_2} z_{2MI} + SMR_4 \cos \gamma_{42} \sin \gamma_{41} \end{Bmatrix} \quad (B37)$$

APPENDIX B - Continued

$$\begin{Bmatrix} x_{5MI} \\ y_{5MI} \\ z_{5MI} \end{Bmatrix} = \begin{Bmatrix} \frac{SML_2}{SMR_2} x_{3MI} + SMR_4 \sin \gamma_{52} \cos \gamma_{51} \\ -R_{UT} - R_2 + \frac{SML_2}{SMR_2} (y_{3MI} - R_{UT} - R_2) - SMR_4 \sin \gamma_{51} \\ (-SML_1 + SL_H) \left(1 - \frac{SML_2}{SMR_2}\right) + \frac{SML_2}{SMR_2} z_{3MI} + SMR_4 \cos \gamma_{52} \sin \gamma_{51} \end{Bmatrix} \quad (B38)$$

$$\begin{Bmatrix} x_{6MI} \\ y_{6MI} \\ z_{6MI} \end{Bmatrix} = \begin{Bmatrix} SMR_6 \sin \gamma_{62} \cos \gamma_{61} \\ R_{LT} - R_6 - SMR_6 \sin \gamma_{61} \\ SMR_6 \cos \gamma_{62} \cos \gamma_{61} \end{Bmatrix} \quad (B39)$$

$$\begin{Bmatrix} x_{7MI} \\ y_{7MI} \\ z_{7MI} \end{Bmatrix} = \begin{Bmatrix} SMR_6 \sin \gamma_{72} \cos \gamma_{71} \\ -R_{LT} + R_6 - SMR_6 \sin \gamma_{71} \\ SMR_6 \cos \gamma_{72} \cos \gamma_{71} \end{Bmatrix} \quad (B40)$$

$$\begin{Bmatrix} x_{8MI} \\ y_{8MI} \\ z_{8MI} \end{Bmatrix} = \begin{Bmatrix} \frac{SML_6}{SMR_6} x_{6MI} + SMR_8 \sin \gamma_{82} \cos \gamma_{81} \\ R_{LT} - R_6 + \frac{SML_6}{SMR_6} (y_{6MI} - R_{LT} + R_6) - SMR_8 \sin \gamma_{81} \\ \frac{SML_6}{SMR_6} z_{6MI} + SMR_8 \cos \gamma_{82} \cos \gamma_{81} \end{Bmatrix} \quad (B41)$$

$$\begin{Bmatrix} x_{9MI} \\ y_{9MI} \\ z_{9MI} \end{Bmatrix} = \begin{Bmatrix} \frac{SML_6}{SMR_6} x_{7MI} + SMR_8 \sin \gamma_{92} \cos \gamma_{91} \\ -R_{LT} + R_6 + \frac{SML_6}{SMR_6} (y_{7MI} + R_{LT} - R_6) - SMR_8 \sin \gamma_{91} \\ \frac{SML_6}{SMR_6} z_{7MI} + SMR_8 \cos \gamma_{92} \cos \gamma_{91} \end{Bmatrix} \quad (B42)$$

Time derivatives of these coordinates can be easily found remembering that segment dimensions are constants for a given model man.

The required position coordinates (denoted by a bar) of the overall mass center are expressed as

$$\bar{x}_{MI} \equiv \frac{\sum_{j=1}^9 m_j x_{jMI}}{m_T} \quad \bar{y}_{MI} \equiv \frac{\sum_{j=1}^9 m_j y_{jMI}}{m_T} \quad \bar{z}_{MI} \equiv \frac{\sum_{j=1}^9 m_j z_{jMI}}{m_T} \quad (B43)$$

where  $m_T$ , total mass of the man, is  $\sum_{j=1}^9 m_j$ . Time derivatives for equations (B43) are easily found, with the values of  $m_T$  and  $m_j$  being constant.

The mass center coordinates ( $x_M, y_M, z_M$ ) for the  $j$ th segment ( $j = 1, 2, \dots, 9$ ) are found by

$$\begin{Bmatrix} x_{Mj} \\ y_{Mj} \\ z_{Mj} \end{Bmatrix} = \begin{Bmatrix} x_{jMI} - \bar{x}_{MI} \\ y_{jMI} - \bar{y}_{MI} \\ z_{jMI} - \bar{z}_{MI} \end{Bmatrix} \quad (B44)$$

or

$$\{r_{Mj}\} = \{r_{jMI}\} - \{r_{MI}\} \quad (B45)$$

Derivatives are

$$\{\dot{r}_{Mj}\} = \{\dot{r}_{jMI}\} - \{\dot{r}_{MI}\} \quad (B46)$$

and

$$\{\ddot{r}_{Mj}\} = \{\ddot{r}_{jMI}\} - \{\ddot{r}_{MI}\} \quad (B47)$$

APPENDIX B – Continued

Specification of functions for the Euler angles  $\gamma_j$  and the translation of the  $X_{MI}, Y_{MI}, Z_{MI}$ -origin are required to express the motion of the model man.

Disturbance Torques for Man's Angular Motion

The disturbance torque resulting from angular motions of the model man can be readily derived in the  $X_M, Y_M, Z_M$ -axes system, which moves with the man's torso and has its origin at the man's center of mass. The torque  $\{T\}$  in the spacecraft coordinate system is related to the torque  $\{T_M\}$  acting on the man in the  $X_M, Y_M, Z_M$ -system by the transformation

$$\{T\} = -[D_1] \{T_M\} \quad (B48)$$

where

$$\{T_M\} = \frac{d\{H_M\}}{dt} \quad (B49)$$

and  $\{H_M\}$  is now expressed in the man's coordinate system. The man's angular momentum can be written as

$$\{H_M\} = [I_M] \{\Omega_M\} + \sum_{j=2}^9 [D_j] [I_j] [D_j]^{-1} \{\Omega_j\} + \sum_{j=1}^9 [m_j] [r_j] \{\dot{r}_j\} \quad (B50)$$

where  $[I_M]$  is the instantaneous inertia matrix of the man, considering all segments,  $[I_j]$  are the principal inertia matrices for the limbs moving relative to the torso,  $\{\Omega_M\}$  is the total angular velocity vector of the torso, and  $\{\Omega_j\}$  are the angular velocities of the body segments 2 to 9 relative to the torso.

Substitution of equation (B50) into equation (B49) gives

$$\begin{aligned} \{T_M\} = & [I_M] \{\dot{\Omega}_M\} + [\dot{I}_M] \{\Omega_M\} + [\Omega_M] [I_M] \{\Omega_M\} + \sum_{j=2}^9 \left[ \left( [D_j] [I_j] \right. \right. \\ & \left. \left. - [D_j] [I_j] [D_j]^{-1} [\dot{D}_j] + [\Omega_M] [D_j] [I_j] \right) [D_j]^{-1} \{\Omega_j\} \right. \\ & \left. + [D_j] [I_j] [D_j]^{-1} \{\dot{\Omega}_j\} \right] + \sum_{j=1}^9 m_j \left( [r_j] \{\ddot{r}_j\} + [\Omega_M] [r_j] \{\dot{r}_j\} \right) \end{aligned} \quad (B51)$$

Expressions for the angular velocity vectors for the man's limbs and torso are needed for the evaluation of equation (B51). The total angular velocity of the torso is given by

APPENDIX B - Continued

$$\{\Omega_M\} = [D_1]^{-1}\{\Omega\} + \left\{ \begin{array}{l} \dot{\gamma}_{11} - \dot{\gamma}_{13} \sin \gamma_{12} \\ \dot{\gamma}_{12} \cos \gamma_{11} + \dot{\gamma}_{13} \sin \gamma_{11} \cos \gamma_{12} \\ \dot{\gamma}_{13} \cos \gamma_{12} \cos \gamma_{11} - \dot{\gamma}_{12} \sin \gamma_{11} \end{array} \right\} \quad (B52)$$

while the angular velocities of the limbs relative to the torso are

$$\Omega_j = \left\{ \begin{array}{l} \dot{\gamma}_{j1} \cos \gamma_{j2} \\ \dot{\gamma}_{j2} \\ -\dot{\gamma}_{j1} \sin \gamma_{j2} \end{array} \right\} \quad (j = 2, 3, \dots, 9) \quad (B53)$$

The moments and products of inertia for the model man are given by the matrix relation

$$[I_M] = ([I_1] + [\Delta I_1]) + \sum_{j=2}^9 ([D_j][I_j][D_j]^{-1} + [\Delta I_j]) \quad (B54)$$

where

$$[I_M] = \begin{bmatrix} I_{XM} & -I_{YXM} & -I_{ZXM} \\ -I_{XYM} & I_{YM} & -I_{ZYM} \\ -I_{XZM} & -I_{YZM} & I_{ZM} \end{bmatrix} \quad (B55)$$

$$[I_j] = \begin{bmatrix} I_{Xj} & 0 & 0 \\ 0 & I_{Yj} & 0 \\ 0 & 0 & I_{Zj} \end{bmatrix} \quad (j = 1, 2, \dots, 9) \quad (B56)$$

and

$$[\Delta I_j] = m_j \begin{bmatrix} y_{Mj}^2 + z_{Mj}^2 & -x_{Mj}y_{Mj} & -x_{Mj}z_{Mj} \\ -x_{Mj}z_{Mj} & x_{Mj}^2 + z_{Mj}^2 & -y_{Mj}z_{Mj} \\ -x_{Mj}z_{Mj} & -y_{Mj}z_{Mj} & x_{Mj}^2 + y_{Mj}^2 \end{bmatrix} \quad (j = 1, 2, \dots, 9) \quad (B57)$$

Values of  $[D_j]$  and  $x_{Mj}, y_{Mj}, z_{Mj}$  have been developed previously.

Use of the model inertias from equation (B54) and their time derivatives, along with the angular velocities from equations (B52) and (B53) and their time derivatives allows

## APPENDIX B – Concluded

the determination of  $\{T_M\}$  in equation (B51), and hence the torque  $\{T\}$  exerted on the spacecraft by man in equation (B48). The total moment applied to the spacecraft can then be computed by using equation (B5).

## REFERENCES

1. Davidson, John R.: The Effect of Random Internal Motions on the Angular Orientation of a Free Body With Limit Control. Ph. D. Thesis, Virginia Polytech. Inst., May 1968.
2. Santschi, W. R.; DuBois, J.; and Omoto, C.: Moments of Inertia and Centers of Gravity of the Living Human Body. AMRL-TDR-63-36, U.S. Air Force, May 1963.
3. Dempster, Wilfred Taylor: Space Requirements of the Seated Operator - Geometrical, Kinematic, and Mechanical Aspects of the Body With Special Reference to the Limbs. WADC TR-55-159, U.S. Air Force, July 1955.
4. Hertzberg, H. T. E.; Daniels, G. S.; and Churchill, E.: Anthropometry of Flying Personnel - 1950. WADC Tech. Rep. 52-321, U.S. Air Force, Sept. 1954. (Available from DDC as AD 47 953.)
5. Hanavan, Ernest P., Jr.: A Mathematical Model of the Human Body. AMRL-TR-64-102, U.S. Air Force, Oct. 1964. (Available from DDC as AD 608 463.)
6. Barter, James T.: Estimation of the Mass of Body Segments. WADC Tech. Rep. 57-260, DDC Doc. No. 118 222, U.S. Air Force, Apr. 1957.
7. Hendricks, T. C.; Johnson, C. H.; and Kirch, D. L.: Crew Motion Data Analysis. ED-2002-644 (Contract NAS 8-24000), Martin Marietta Corp., Oct. 14, 1968.
8. Murrish, C. H.; and Smith, G. W.: Apollo Applications Program Crew Motion Experiment - Program Definition and Design Development. Contract NAS 1-7276, Martin Marietta Corp., Mar. 1968. (Available as NASA CR-66599.)
9. Chubb, W. B.; and Seltzer, S. M.: Skylab Attitude and Pointing Control System. NASA TN D-6068, 1971.
10. Fuhrmeister, W. F.; and Fowler, J. L.: Experimental Study of Dynamic Effects of Crew Motion in a Manned Orbital Research Laboratory (MORL). Contract No. NAS 1-5937, Douglas Aircraft Co., Inc., Oct. 1966. (Available as NASA CR-66186.)
11. Tewell, J. R.; and Murrish, C. H.: Engineering Study and Experiment Definition for an Apollo Applications Program Experiment on Vehicle Disturbances Due to Crew Activity. Contract No. NAS 1-6713, Martin Marietta Corp., Mar. 1967. (Available as NASA CR-66277.)



004 001 C1 U 31 720107 S00903DS  
DEPT OF THE AIR FORCE  
AF WEAPONS LAB (AFSC)  
TECH LIBRARY/WLOL/  
ATTN: E LOU BOWMAN, CHIEF  
KIRTLAND AFB NM 87117

POSTMASTER: If Undeliverable (Section 158  
Postal Manual) Do Not Return

*"The aeronautical and space activities of the United States shall be conducted so as to contribute . . . to the expansion of human knowledge of phenomena in the atmosphere and space. The Administration shall provide for the widest practicable and appropriate dissemination of information concerning its activities and the results thereof."*

— NATIONAL AERONAUTICS AND SPACE ACT OF 1958

## NASA SCIENTIFIC AND TECHNICAL PUBLICATIONS

**TECHNICAL REPORTS:** Scientific and technical information considered important, complete, and a lasting contribution to existing knowledge.

**TECHNICAL NOTES:** Information less broad in scope but nevertheless of importance as a contribution to existing knowledge.

**TECHNICAL MEMORANDUMS:** Information receiving limited distribution because of preliminary data, security classification, or other reasons.

**CONTRACTOR REPORTS:** Scientific and technical information generated under a NASA contract or grant and considered an important contribution to existing knowledge.

**TECHNICAL TRANSLATIONS:** Information published in a foreign language considered to merit NASA distribution in English.

**SPECIAL PUBLICATIONS:** Information derived from or of value to NASA activities. Publications include conference proceedings, monographs, data compilations, handbooks, sourcebooks, and special bibliographies.

**TECHNOLOGY UTILIZATION PUBLICATIONS:** Information on technology used by NASA that may be of particular interest in commercial and other non-aerospace applications. Publications include Tech Briefs, Technology Utilization Reports and Technology Surveys.

*Details on the availability of these publications may be obtained from:*

**SCIENTIFIC AND TECHNICAL INFORMATION OFFICE**

**NATIONAL AERONAUTICS AND SPACE ADMINISTRATION**

**Washington, D.C. 20546**